



HAL
open science

A Large West Antarctic Ice Sheet Explains Early Neogene Sea-Level Amplitude

J. Marschalek, L. Zurli, F. Talarico, T. van de Flierdt, P. Vermeesch, A. Carter, F. Beny, V. Bout-Roumazeilles, F. Sangiorgi, S. Hemming, et al.

► **To cite this version:**

J. Marschalek, L. Zurli, F. Talarico, T. van de Flierdt, P. Vermeesch, et al.. A Large West Antarctic Ice Sheet Explains Early Neogene Sea-Level Amplitude. *Nature*, 2021, 600 (7889), pp.450-455. 10.1038/s41586-021-04148-0 . hal-03796588

HAL Id: hal-03796588

<https://sde.hal.science/hal-03796588>

Submitted on 10 Oct 2022

HAL is a multi-disciplinary open access archive for the deposit and dissemination of scientific research documents, whether they are published or not. The documents may come from teaching and research institutions in France or abroad, or from public or private research centers.

L'archive ouverte pluridisciplinaire **HAL**, est destinée au dépôt et à la diffusion de documents scientifiques de niveau recherche, publiés ou non, émanant des établissements d'enseignement et de recherche français ou étrangers, des laboratoires publics ou privés.

1 **A Large West Antarctic Ice Sheet Explains Early Neogene Sea-Level Amplitude**

2 *J.W. Marschalek^{1*}, L. Zurli², F. Talarico², T. van de Flierdt¹, P. Vermeesch³, A. Carter⁴, F. Beny⁵, V.*
3 *Bout-Roumazelles⁵, F. Sangiorgi⁶, S.R. Hemming⁷, L.F. Pérez^{8,9}, F. Colleoni¹⁰, J. Prebble¹¹, T.E.*
4 *van Peer^{3,12}, M. Perotti², A.E. Shevenell¹³, I. Browne¹³, D.K. Kulhanek¹⁴, R. Levy^{11,15}, D. Harwood¹⁶,*
5 *N.B. Sullivan¹⁷, S.R. Meyers¹⁷, E.M. Griffith¹⁸, C.-D. Hillenbrand⁸, E. Gasson¹⁹, M.J. Siegert^{1,20}, B.*
6 *Keisling⁷, K.J. Licht²¹, G. Kuhn²², J.E. Dodd²³, C. Boshuis⁶, L. De Santis¹⁰, R.M. McKay¹⁵*

7 ¹Department of Earth Science and Engineering, Imperial College London, Exhibition Road, London, SW7 2AZ, UK;
8 j.marschalek18@imperial.ac.uk

9 ²Department of Physical, Earth and Environmental Sciences, University of Siena, via Laterina 8, 53100 Siena, Italy

10 ³Department of Earth Sciences, University College London, UK

11 ⁴Department of Earth and Planetary Sciences, Birkbeck, University of London, UK

12 ⁵Laboratoire d'Océanologie et de Géosciences, UMR 8187 CNRS/Univ Lille/ULCO, 8 Cité scientifique, F-59655
13 Villeneuve d'Ascq, France.

14 ⁶ Department of Earth Sciences, Marine Palynology and Paleoceanography, University of Utrecht, The Netherlands

15 ⁷Lamont-Doherty Earth Observatory of Columbia University Palisades, New York, USA

16 ⁸British Antarctic Survey, High Cross, Madingley Road, Cambridge, UK

17 ⁹Department of Marine Geology, C.F Møllers Allé 8, Bygning 1110, Office: 226 DK-8000 Aarhus C, Denmark.

18 ¹⁰Geophysics Division, National Institute of Oceanography and Applied Geophysics – OGS, Trieste, Italy

19 ¹¹GNS Science, Lower Hutt, New Zealand.

20 ¹²National Oceanography Centre Southampton, University of Southampton Waterfront Campus, Southampton, UK

21 ¹³College of Marine Science, University of South Florida, St. Petersburg, FL, 33701, USA

22 ¹⁴International Ocean Discovery Program, Texas A&M University, TX, USA

23 ¹⁵Antarctic Research Centre, Victoria University of Wellington, Wellington, New Zealand

24 ¹⁶Department of Earth and Atmospheric Sciences, University of Nebraska-Lincoln, Lincoln, NE 68588-0340, USA

25 ¹⁷Department of Geoscience, University of Wisconsin-Madison, Madison, WI 53706, USA

26 ¹⁸School of Earth Sciences, Ohio State University, Columbus, OH 43210, USA

27 ¹⁹Centre for Geography and Environmental Sciences, University of Exeter, Penryn Campus, Cornwall, UK.

28 ²⁰Grantham Institute, Imperial College London, Exhibition Road, South Kensington, London SW7 2AZ, UK

29 ²¹Department of Earth Sciences, Indiana University Purdue University Indianapolis, Indianapolis, USA

30 ²²Alfred Wegener Institute, Helmholtz Centre for Polar and Marine Research, 27568 Bremerhaven, Germany

31 ²³Department of Geology, Northern Illinois University, DeKalb, Illinois 60115, USA

32 **Early to Middle Miocene sea-level oscillations of approximately 40-60 m estimated from far-**
33 **field records^{1,2,3} are interpreted to reflect the loss of virtually all East Antarctic ice during peak**
34 **warmth². This contrasts with ice-sheet model experiments suggesting most terrestrial ice in**
35 **East Antarctica was retained even during the warmest intervals of the Middle Miocene^{4,5}. Data**
36 **and model outputs can be reconciled if a large West Antarctic Ice Sheet (WAIS) existed and**
37 **expanded across most of the outer continental shelf during the Early Miocene, accounting for**
38 **maximum ice-sheet volumes. Here, we provide the earliest geological evidence proving large**
39 **WAIS expansions occurred during the Early Miocene (~17.72-17.40 Ma). Geochemical and**
40 **petrographic data show glacial marine sediments recovered at International Ocean Discovery**
41 **Program (IODP) Site U1521 in the central Ross Sea derive from West Antarctica, requiring the**
42 **presence of a WAIS covering most of the Ross Sea continental shelf. Seismic, lithological and**
43 **palynological data reveal the intermittent proximity of grounded ice to Site U1521. The erosion**
44 **rate calculated from this sediment package greatly exceeds the long-term mean, implying rapid**
45 **erosion of West Antarctica. This interval therefore captures a key step in the genesis of a**
46 **marine-based WAIS and a tipping point in Antarctic ice-sheet evolution.**

47 **Introduction**

48 Reconstructing past Antarctic ice sheet change informs predictions of the continent's contribution to
49 future sea-level rise^{6,7}. Since the 1970s, drilling efforts proximal to Antarctica have revealed the
50 general Cenozoic evolution of Antarctic glaciation^{8,9,10,11}, but fundamental steps in the development
51 of the ice sheets remain poorly constrained. One key uncertainty is the timing of West Antarctic Ice
52 Sheet (WAIS) initiation and expansion across the outer continental shelf. Deep-sea benthic

53 foraminifer oxygen isotope records and Antarctic abyssal plain sedimentary sequences suggested
54 WAIS formation occurred in the Late Miocene or early Pliocene^{12,13}. However, drilling from the
55 Antarctic margin^{11,14,15} and ice-sheet modelling studies^{4,5,16} have raised the possibility that WAIS
56 expansions into areas below sea-level could have occurred during the Early Miocene or earlier,
57 facilitated by a subaerial West Antarctic topography^{17,18}.

58 Without widespread WAIS expansions across the continental shelf in the Early Miocene, maximum
59 ice volumes are low enough that global sea-level fluctuations of ~40-60 m estimated from far-field
60 stratigraphic records¹ and oxygen isotope-derived ice volume estimates^{2,3} require the near complete
61 loss of the East Antarctic Ice Sheet (EAIS) during the warmest Middle Miocene periods². Such an
62 outcome is incompatible with current ice-sheet model outputs, which suggest retention of most
63 terrestrial East Antarctic ice even during the warmest feasible Middle Miocene environmental
64 conditions⁴. This is mainly due to hysteresis effects driven by height-mass balance feedbacks; once
65 the ice sheet is present, parts of it can be retained in a climate warmer than that which would permit
66 ice-sheet inception on an ice-free landscape^{4,19}.

67 Marine sediments, deposited on the continental shelf of the Ross Sea, can reveal whether the WAIS
68 expanded across the continental shelf during the Early Miocene. However, ice proximal geological
69 records have been hampered by poor recovery, unconformities, and/or influence from East
70 Antarctica^{9,10,11}. Seismic data suggest that significant volumes of lower Miocene glacimarine
71 sediment exist around the West Antarctic margin^{20,21,22,23}. However, seismic data require constraints
72 from drilling to determine the age of the sediments, and to differentiate between detritus from
73 continental-scale ice-sheet expansion and local ice caps on (paleo)topographic highs^{22,23}.

74 Consequently, WAIS grounding across the Ross Sea shelf is only clear in seismic data after the
75 Middle Miocene Climate Transition (~14 Ma)^{24,25}; it remains uncertain whether there were earlier
76 WAIS expansions across the Ross Sea shelf.

77 **IODP Site U1521 and Provenance Approach**

78 IODP Expedition 374 Site U1521 (75°41.0' S, 179°40.3' W; 562 m water depth) was drilled to 650.1
79 metres below sea floor (mbsf) in the Pennell Basin on the outer continental shelf of the Ross Sea
80 (Fig. 1). The site was drilled in a region that ice-sheet models indicate is one of the last locations
81 where ice grounds during glacial maxima, making it an ideal location to assess the timing of past
82 WAIS expansions onto the outer continental shelf^{4,16,26}. The sediments from the base of the borehole
83 up to 209.17 mbsf are split into four chronostratigraphic sequences (1-4; Fig. 2) which constitute an
84 expanded lower Miocene section (~18 to ~16.3 Ma; see Supplementary Material for details) with
85 73% recovery. These sediments provide a unique window for detailed analysis of ice-sheet behaviour
86 immediately before the onset of the Miocene Climate Optimum (MCO, ~17 Ma; Fig. 2; Extended
87 Data Fig. 1; Extended Data Table 1).

88 Site U1521 sediments below 209.17 mbsf are predominantly muddy to sandy diamictites, often
89 interbedded with thin laminae and beds of mudstone (see Supplementary Material for details)²⁶.
90 Palynological counts on 23 samples revealed sparse palynomorphs in Sequences 1 and 4A, common
91 reworked dinoflagellate cysts in Sequence 2, and evidence for high biological productivity in
92 Sequence 3B (Extended Data Fig. 2; Supplementary Material). These lithological and
93 paleontological data from Sequences 1, 2, 3A and 4A indicate an ice-proximal glacimarine (and
94 potentially subglacial) setting, while data from Sequence 3B suggest an ice-distal setting. Notably,
95 the ~190 m thick succession of Sequence 2, containing a high proportion of reworked dinoflagellate
96 cysts, was deposited rapidly (0.592 mm a⁻¹) within a ~317 kyr interval spanning ~17.72-17.40 Ma
97 (Extended Data Fig. 1).

98 Through comparison with terrestrial rock outcrops, the sediments recovered at Site U1521 were
99 traced back to their source regions. A differing geological history of the rocks beneath the EAIS and
100 WAIS (Fig. 1) gives the sediment eroded by each ice sheet a distinct geochemical, petrological and
101 mineralogical composition, allowing expansions of the EAIS and WAIS to be distinguished. To
102 avoid bias towards, or omission of, any lithologies, we applied multiple sediment provenance

103 proxies²⁷. Specifically, we analysed the detrital fine fraction of 37 samples for neodymium (Nd) and
104 strontium (Sr) isotope compositions (<63 μm) and 23 samples for clay mineralogy (<2 μm). Eight
105 samples were also processed for U-Pb dating of detrital zircons (<300 μm) and five for $^{40}\text{Ar}/^{39}\text{Ar}$
106 dating of detrital hornblende grains (150-300 μm). Additionally, the petrological composition of
107 15,740 clasts >2 mm was identified down-core (Extended Data Fig. 3).

108 **Evidence for Early Miocene WAIS Growth**

109 At Site U1521, detrital ϵ_{Nd} values are consistently more radiogenic (higher) in Sequence 2 compared
110 to the sediments above and below (Fig. 2e), implying a contribution from a more radiogenic end
111 member. This end member can be traced to beneath the WAIS; the ϵ_{Nd} values, ranging between -7.2
112 and -5.9, are in good agreement with measurements of Upper Quaternary diamicts from the eastern
113 Ross Sea shelf, adjacent to West Antarctica²⁸. Here, the radiogenic end member is hypothesised to be
114 the Cenozoic alkali volcanic rocks of Marie Byrd Land, West Antarctica (Extended Data Fig. 4)²⁸.
115 Subaerial outcrops of the Marie Byrd Land volcanic province are limited, but magnetic and gravity
116 anomalies associated with subglacial cone-shaped structures indicate the presence of numerous
117 subglacial volcanoes (Fig. 1)²⁹. We hypothesize that the Marie Byrd Land volcanic province is the
118 more radiogenic end member in Sequence 2. Conversely, the less radiogenic (lower) ϵ_{Nd} values seen
119 in Sequences 1, 3A and 4A reflect a mixture of lithologies present in the (East Antarctic)
120 Transantarctic Mountains and fall within the range of Upper Quaternary Ross Sea tills of
121 Transantarctic Mountain provenance (Extended Data Figs. 4, 5)^{28,30}. These less radiogenic sediments
122 also show higher and more variable magnetic susceptibility (Fig. 2)²⁶. The patterns seen in the ϵ_{Nd}
123 data are broadly mirrored by detrital Sr isotope compositions (Extended Data Fig. 2).
124 Single-grain geochronology/thermochronology and clast petrography provide insights into specific
125 source terranes. In the Transantarctic Mountains, Precambrian rocks were affected by the pervasive
126 Ross Orogeny (615-470 Ma), which was accompanied by intrusive felsic magmatism

127 (Supplementary Material)³¹. Zircon age populations from Sequences 1, 3A and 4A show a strong
128 peak towards the earlier part of the Ross Orogeny (595 to 535 Ma) and a 6 to 21% population of
129 Archaean and Paleoproterozoic (>1600 Ma) zircon grains (Figs. 1, 3). These features, together with a
130 lack of grains younger than 250 Ma, resemble data from moraines in the Transantarctic
131 Mountains^{32,33,34}. Clasts in sequences 1, 3A and 4A also correlate with rocks in the Transantarctic
132 Mountains, with lithologies including common felsic granitoids and meta-sediments alongside rarer
133 limestones, marbles and sandstones (Extended Data Fig. 3)³¹. Although a relatively minor
134 component, dolerite clasts are found throughout Sequences 1, 3A and 4A (Fig. 2g) and can be traced
135 to the Jurassic Ferrar Group, which predominantly crops out in the Transantarctic Mountains (Fig. 1).
136 Furthermore, rare *Protohaploxylinus* pollen, a distinctive component of the Permian Beacon
137 Supergroup in the Transantarctic Mountains, are observed in Sequence 3A³⁵. Overall, the sediments
138 comprising Site U1521 Sequences 1, 3A and 4A are predominantly sourced from erosion of the
139 Transantarctic Mountains in East Antarctica.

140 In contrast, Sequence 2 is characterized by the highest ϵ_{Nd} values and contains zircons with
141 Cretaceous (~100 Ma) U-Pb ages (n = 16; Fig. 3a). Such ages are indicative of a West Antarctic
142 provenance as they are presently only found beneath the modern Siple Coast ice streams, including
143 Kamb Ice Stream and those closer to Marie Byrd Land^{33,36}. The age spectra of samples from
144 Sequence 2 share other features with data from the Siple Coast ice streams, including a broad
145 Triassic (~240-190 Ma) age peak, few pre-Mesoproterozoic zircons (<5 % of grains) and a young
146 (~515-505 Ma) Ross Orogeny peak (Fig. 3)³³. Detrital hornblende $^{40}Ar/^{39}Ar$ ages from Sequence 2
147 further corroborate a West Antarctic provenance. Unlike zircon grains, which can survive multiple
148 sedimentary cycles, hornblende grains are less resistant to weathering. The absence of Grenvillian
149 (~1100-900 Ma) ages in the Sequence 2 hornblende sample (Extended Data Fig. 6) therefore
150 suggests a West Antarctic provenance, as Grenville-age rocks are absent there³⁷. The scarcity of
151 Ferrar Group dolerite clasts, common in the Transantarctic Mountains, is also consistent with a West

152 Antarctic provenance (Figs. 1, 2), as is a high proportion of smectite in the clay fraction at the bottom
153 of Sequence 2 ($\leq 58\%$; Extended Data Fig. 3), with smectite percentages similar to Quaternary
154 sediments in the eastern Ross Sea³⁸. Additionally, Sequence 2 contains evidence for recycling of
155 older marine detritus, most likely from the lower Cenozoic rift-fill strata that exist in the eastern Ross
156 Sea region of the West Antarctic Rift System²¹. This is inferred from the dominance of reworked
157 Eocene-Oligocene species in the diatom and spore-pollen assemblages²⁶, alongside the common (13-
158 21%) reworked Eocene-Oligocene marine dinocysts, which are rare ($< 1.5\%$) in younger sediments
159 (Extended Data Fig. 2).

160 Smectite abundance declines significantly up-section within Sequence 2 and is accompanied by an
161 increase in the proportion of basalt clasts (Extended Data Fig. 7). This anticorrelation is unexpected
162 given that smectite is a weathering product of basalt and volcanic rocks. We infer that lower in
163 Sequence 2, basaltic bedrock was predominantly weathered to smectite and was thus largely
164 confined to the finer grain size fractions. Over time, this more weathered regolith layer was removed,
165 leading to erosion of progressively more pristine continental detritus containing more basalt clasts.
166 This scenario is supported by more radiogenic ϵ_{Nd} values measured in the $< 63 \mu\text{m}$ fraction lower in
167 Sequence 2 (Fig. 2, Extended Data Fig. 7), as Marie Byrd Land basalts are more radiogenic than
168 other lithologies (Extended Data Fig. 5). Sequence 2 (17.72-17.40 Ma) could therefore record an
169 advance of the WAIS over parts of West Antarctica which had not been covered by grounded ice for
170 an extended period.

171 Further evidence for WAIS expansion can be found in seismic data, which can trace the sediment
172 package deposited at Site U1521 between 17.72 and 17.40 Ma (Sequence 2) across the Ross Sea
173 continental shelf²³. The sediment package, which is thicker towards the eastern Ross Sea (i.e., West
174 Antarctica), contains glacial features including widespread progradational wedges and high relief
175 morainal banks^{20,21,23}. Coupled with the lithological and palynological evidence for ice proximity at
176 Site U1521, this shows marine-terminating ice was present. Transport of large volumes of West

177 Antarctic detritus as far west as the Pennell Basin in the central Ross Sea is evident in our
178 provenance data, which, alongside common reworked marine microfossils, proves this marine-
179 terminating ice derived from an Early Miocene WAIS which intermittently extended across most of
180 the outer continental shelf.

181 Our data therefore reveal WAIS expansions across the Ross Sea continental shelf date back to at
182 least 17.72 Ma, which is significantly earlier than previously suggested^{12,13,23,24,39}. Advance of the
183 WAIS into marine-based areas (i.e., regions grounded mainly below sea level) at 17.72-17.40 Ma is
184 supported by a corresponding period of high sensitivity of the marine $\delta^{18}\text{O}$ record to obliquity
185 forcing (Fig. 2i). High obliquity sensitivity is considered a proxy for enhanced ice-sheet sensitivity to
186 ocean dynamics and thus the presence of marine-based ice¹⁵.

187 **Birth of a Marine-Based WAIS**

188 The mean erosion rate for the WAIS catchments draining to the Ross Sea between 17.72 and 17.40
189 Ma can be estimated using the volume of the corresponding seismic package east of Site U1521²³.
190 Assuming that, at the time of deposition, the area of the Ross Sea drainage sector of the WAIS was
191 approximately the same as today ($\pm 20\%$), the inferred sediment volume requires a mean catchment
192 erosion of approximately 87 m in ~ 317 kyr (Extended Data Table 2). The mean erosion rate of
193 ~ 0.275 mm a^{-1} during this interval greatly exceeds the long-term mean rate of 0.012 mm a^{-1}
194 calculated for this part of the WAIS between 23 and 14 Ma¹⁸; even when the full uncertainty is taken
195 into account (Extended Data Table 2), it is still more than an order of magnitude higher. This
196 highlights the 17.72 to 17.40 Ma interval as one of unusually rapid erosion, with erosion rates
197 comparable to modern subpolar to temperate glacial catchments⁴⁰. Transporting this large volume of
198 subglacially eroded debris quickly to the WAIS margin required abundant meltwater at the ice sheet
199 bed⁴¹, as well as fast-flowing ice streams that extended into marine settings where broad deposition
200 took place. Ocean temperatures must therefore have been sufficiently cool to permit the advance of

201 marine-based ice, yet atmospheric conditions must have remained warm enough to provide sufficient
202 precipitation to drive dynamic ice flow and enhanced basal erosion⁴.

203 Since most of West Antarctica, apart from Marie Byrd Land, was thermally subsiding throughout the
204 Miocene¹⁸, the high erosion rate at 17.72 to 17.40 Ma is unlikely to have been driven by tectonic
205 uplift. The eroded sediments therefore reflect ice expansion and enhanced glacial incision of the
206 terrestrial West Antarctic hinterland, plus infilling of the Ross Sea basins. This erosive event
207 occurred at a time when topographic reconstructions indicate a transition from a terrestrial West
208 Antarctic topography (23 Ma) to a largely submarine West Antarctic topography (14 Ma)¹⁸. The
209 timing and large volume of sediment deposited in Sequence 2 at Site U1521 suggests that the 17.72
210 to 17.40 Ma interval records a critical step in the transition of the WAIS from a largely terrestrial ice
211 sheet to one that was primarily marine-based. This significant alteration to West Antarctic
212 topography occurred just prior to major changes affecting the Antarctic cryosphere and global
213 climate during the MCO^{2,11}. Subglacial erosion may therefore have driven changes in ice-sheet
214 evolution and behaviour as, after ~17.40 Ma, a greater submarine area in central West Antarctica
215 would have made the mass-balance control of the WAIS more sensitive to external drivers such as
216 sea level and oceanic forcing^{5,16}. We propose that ice retreat at the onset of the MCO may be
217 partially attributable to the crossing of this topographic tipping point and that Sequence 2 records the
218 birth of a marine-based WAIS. This event dates to well before 14 Ma, the time slice at which
219 topographic reconstructions first show a largely sub-marine West Antarctica¹⁸.

220 **Sea-Level Reconciliation**

221 Grounded ice flowing from West Antarctica was close to Site U1521 towards the end of the Early
222 Miocene. We therefore validate recent modelling studies suggesting that an ice sheet nucleating on a
223 partially terrestrial West Antarctica could expand extensively into the marine realm under Early
224 Miocene climatic and paleotopographic conditions^{4,5,16}. Our data are consistent with an ice extent

225 similar to, or exceeding, the largest modelled Early to Middle Miocene Antarctic ice sheets (Fig. 1),
226 containing ice volumes of approximately 80 m sea-level equivalent (SLE) depending on the
227 topographic reconstruction used^{4,5,16}. This expanded WAIS contained approximately 14-15 m SLE of
228 ice, but also acted to buttress the EAIS resulting in significantly larger-than-present ice volumes^{4,16}.
229 These maximum ice volume constraints indicate that far-field sea-level amplitudes of ~40-60 m did
230 not require the loss of nearly all terrestrial East Antarctic ice during subsequent warm periods during
231 the MCO^{1,2,3}, consistent with modelled EAIS hysteresis effects⁴. By providing the earliest conclusive
232 evidence for a large marine-based WAIS, our data also dispel long-held inferences that a WAIS, able
233 to significantly impact global eustasy and climate, was not present until the Middle or Late
234 Miocene^{12,13,39}.

235 References

- 236 1. Kominz, M. A. et al. Miocene relative sea level on the New Jersey shallow continental shelf
237 and coastal plain derived from one-dimensional backstripping: A case for both eustasy and
238 epeirogeny. *Geosphere* 12, 1437-1456 (2016).
- 239 2. Miller, K. G. et al. Cenozoic sea-level and cryospheric evolution from deep-sea
240 geochemical and continental margin records. *Science advances* 6, p. eaaz1346 (2020).
- 241 3. Pekar, S. F., & DeConto, R. M. High-resolution ice-volume estimates for the early
242 Miocene: Evidence for a dynamic ice sheet in Antarctica. *Palaeogeogr., Palaeoclimatol.,*
243 *Palaeoecol.* 231, 101-109 (2006).
- 244 4. Gasson, E., DeConto, R. M., Pollard, D. & Levy, R. H. Dynamic Antarctic ice sheet during
245 the early to mid-Miocene. *Proc. Natl. Acad. Sci. USA* 113, 3459–3464 (2016).
- 246 5. Paxman, G. J., Gasson, E. G., Jamieson, S. S., Bentley, M. J., & Ferraccioli, F. Long-Term
247 Increase in Antarctic Ice Sheet Vulnerability Driven by Bed Topography
248 Evolution. *Geophysical Research Letters* 47, e2020GL090003 (2020).
- 249 6. Masson-Delmotte, V. et al. Information from paleoclimate archives. *Climate change* 383–
250 464 (2013).
- 251 7. Kennicutt, M. C. et al. A roadmap for Antarctic and Southern Ocean science for the next
252 two decades and beyond. *Antarctic Science* 27, 3-18 (2014).
- 253 8. Kennett, J. P. Cenozoic evolution of Antarctic glaciation, the circum-Antarctic Ocean, and
254 their impact on global paleoceanography. *Journal of Geophysical Research* 82, 3843-3860
255 (1977).
- 256 9. Barrett, P. J. Characteristics of pebbles from Cenozoic marine glacial sediments in the Ross
257 Sea (DSDP Sites 270–274) and the South Indian Ocean (Site 268). In *Initial Reports of the*
258 *Deep-Sea Drilling Project* 28, 769-784 (1975).

- 259 10. Passchier, S., & Krissek, L. A. Oligocene–Miocene Antarctic continental weathering record
260 and paleoclimatic implications, Cape Roberts drilling project, Ross Sea,
261 Antarctica. *Palaeogeogr., Palaeoclimatol., Palaeoecol.* 260, 30-40 (2008).
- 262 11. Levy, R. et al. Antarctic ice sheet sensitivity to atmospheric CO₂ variations in the early to
263 mid-Miocene. *Proceedings of the National Academy of Sciences* 113, 3453-3458 (2016).
- 264 12. Zachos, J., Pagani, M., Sloan, L., Thomas, E., & Billups, K. Trends, rhythms, and
265 aberrations in global climate 65 Ma to present. *Science* 292, 686-693 (2001).
- 266 13. Kennett, J.P., and Barker, P.F. Latest Cretaceous to Cenozoic climate and oceanographic
267 developments in the Weddell Sea, Antarctica: an ocean-drilling perspective. *Proc. Ocean
268 Drill. Program Sci. Results* 113, 937–960 (1990). doi:10.2973/odp.proc.sr.113.195.1990
- 269 14. Hauptvogel, D. W., & Passchier, S. Early–Middle Miocene (17–14 Ma) Antarctic ice
270 dynamics reconstructed from the heavy mineral provenance in the AND-2A drill core, Ross
271 Sea, Antarctica. *Global and Planetary Change* 82, 38-50 (2012).
- 272 15. Levy, R. H. et al. Antarctic ice-sheet sensitivity to obliquity forcing enhanced through
273 ocean connections. *Nature Geoscience* 12, 132-137 (2019).
- 274 16. Colleoni, F. et al. Past continental shelf evolution increased Antarctic ice sheet sensitivity to
275 climatic conditions. *Scientific reports* 8, 1-12 (2018).
- 276 17. Wilson, D. S. et al. Antarctic topography at the Eocene-Oligocene boundary, *Palaeogeogr.
277 Palaeoclimatol. Palaeoecol.* 335-336, 24–34 (2012). doi:10.1016/j.palaeo.2011.05.028.
- 278 18. Paxman, G. J., Jamieson, S. S., Hochmuth, K., Gohl, K., Bentley, M. J., Leitchkov, G., &
279 Ferraccioli, F. Reconstructions of Antarctic topography since the Eocene–Oligocene
280 boundary. *Palaeogeogr., Palaeoclimatol., Palaeoecol.* 535 (2019).
- 281 19. Gasson, E. G., & Keisling, B. A. The Antarctic Ice Sheet: A Paleoclimate Modelling
282 Perspective. *Oceanography* 33, 90-100 (2020).
- 283 20. Anderson, J. B., & Bartek, L. R. Cenozoic glacial history of the Ross Sea revealed by
284 intermediate resolution seismic reflection data combined with drill site information. *The
285 Antarctic Paleoenvironment: A Perspective on Global Change: Part One* 56, 231-264
286 (1992).
- 287 21. De Santis, L., Anderson, J. B., Brancolini, G., & Zayatz, I. Seismic record of late Oligocene
288 through Miocene glaciation on the central and eastern continental shelf of the Ross
289 Sea. *Geology and Seismic Stratigraphy of the Antarctic Margin* 68, 235-260 (1995).
- 290 22. Gohl, K. et al. Seismic stratigraphic record of the Amundsen Sea Embayment shelf from
291 pre-glacial to recent times: Evidence for a dynamic West Antarctic Ice Sheet. *Marine
292 Geology* 344, 115-131 (2013).
- 293 23. Pérez, L.F. et al. Early-middle Miocene ice sheet dynamics in the Ross Sea embayment:
294 results from integrated core-log-seismic interpretation. *GSA Bulletin* (2021).
- 295 24. Bart, P. J. Were West Antarctic ice sheet grounding events in the Ross Sea a consequence
296 of East Antarctic ice sheet expansion during the middle Miocene? *Earth and Planetary
297 Science Letters* 216, 93-107 (2003).
- 298 25. Chow, J. M., & Bart, P. J. West Antarctic Ice Sheet grounding events on the Ross Sea outer
299 continental shelf during the middle Miocene. *Palaeogeogr., Palaeoclimatol., Palaeoecol.*
300 198, 169-186 (2003).

- 301 26. McKay, R., De Santis, L., Kulhanek, D. K., and the Expedition 374 Science Party. Ross Sea
302 West Antarctic Ice Sheet History. College Station, Texas, International Ocean Discovery
303 Program, Proceedings of the International Ocean Discovery Program (2019).
- 304 27. Licht, K. J., & Hemming, S. R. Analysis of Antarctic glacial sediment provenance
305 through geochemical and petrologic applications. *Quaternary Science Reviews* 164, 1-24
306 (2017).
- 307 28. Farmer, G. L., Licht, K., Swope, R. J., & Andrews, J. Isotopic constraints on the
308 provenance of fine-grained sediment in LGM tills from the Ross Embayment,
309 Antarctica. *Earth and Planetary Science Letters* 249, 90-107 (2006).
- 310 29. van Wyck de Vries, M., Bingham, R. G., & Hein, A. S. A new volcanic province: an
311 inventory of subglacial volcanoes in West Antarctica. Geological Society, London, Special
312 Publications 461, SP461. 467 (2017).
- 313 30. Farmer, G. L., & Licht, K. J. Generation and fate of glacial sediments in the central
314 Transantarctic Mountains based on radiogenic isotopes and implications for reconstructing
315 past ice dynamics. *Quaternary Science Reviews* 150, 98-109 (2016).
- 316 31. Goodge, J. W. Geological and tectonic evolution of the Transantarctic Mountains, from
317 ancient craton to recent enigma. *Gondwana Research* 80, 50-122 (2020).
- 318 32. Licht, K. J., & Palmer, E. F. Erosion and transport by Byrd Glacier, Antarctica during the
319 last glacial maximum. *Quaternary Science Reviews* 62, 32-48 (2013).
- 320 33. Licht, K. J., Hennessy, A. J., & Welke, B. M. The U-Pb detrital zircon signature of West
321 Antarctic ice stream tills in the Ross embayment, with implications for Last Glacial
322 Maximum ice flow reconstructions. *Antarctic Science* 26, 687-697 (2014).
- 323 34. Bader, N. A., Licht, K. J., Kaplan, M. R., Kassab, C., & Winckler, G. East Antarctic ice
324 sheet stability recorded in a high-elevation ice-cored moraine. *Quaternary Science Reviews*
325 159, 88-102 (2017).
- 326 35. Kyle, R.A. & Schopf, J.M. Permian and Triassic palynostratigraphy of the Victoria Group,
327 Transantarctic Mountains: in Craddock, C., ed., *Antarctic geoscience: Madison*, University
328 of Wisconsin Press, International Union of Geological Sciences, Series B-4, 649–659
329 (1982).
- 330 36. Perotti, M., Andreucci, B., Talarico, F., Zattin, M., & Langone, A. Multianalytical
331 provenance analysis of Eastern Ross Sea LGM till sediments (Antarctica): Petrography,
332 geochronology, and thermochronology detrital data. *Geochemistry, Geophysics,*
333 *Geosystems* 18, 2275-2304 (2017).
- 334 37. Jordan, T. A., Riley, T. R., & Siddoway, C. S. The geological history and evolution of West
335 Antarctica. *Nature Reviews Earth & Environment* 1, 1-17 (2020).
- 336 38. Balshaw-Biddle, K. M. Antarctic glacial chronology reflected in the Oligocene through
337 Pliocene sedimentary section in the Ross Sea (Rice University, 1981).
- 338 39. Westerhold, T. et al. An astronomically dated record of Earth's climate and its
339 predictability over the last 66 million years. *Science* 369, 1383-1387 (2020).
- 340 40. Koppes, M. et al. Observed latitudinal variations in erosion as a function of glacier
341 dynamics. *Nature* 526, 100–103 (2015).
- 342 41. Alley, R. B., Cuffey, K. M., & Zoet, L. K. Glacial erosion: status and outlook. *Annals of*
343 *Glaciology* 60, 1-13 (2019).

- 344 42. Cox S.C., Smith Lyttle B. and the GeoMAP team. SCAR GeoMAP dataset. GNS Science,
345 Lower Hutt, New Zealand. Release v.201907 (2019). <https://doi.org/10.21420/7SH7-6K05>
- 346 43. Morlighem, M. et al. Deep glacial troughs and stabilizing ridges unveiled beneath the
347 margins of the Antarctic ice sheet. *Nat. Geosci.* 13, 132–137 (2020).
348 <https://doi.org/10.1038/s41561-019-0510-8>
- 349 44. Mouginot, J., Scheuchl, B. and Rignot, E. MEaSURES Antarctic Boundaries for IPY 2007-
350 2009 from Satellite Radar, Version 2. Boulder, Colorado USA. NASA National Snow and
351 Ice Data Center Distributed Active Archive Center (2017). doi:
352 <https://doi.org/10.5067/AXE4121732AD>.
- 353 45. Rignot, E., Jacobs, S. S., Mouginot, J. & B. Scheuchl. Ice-shelf melting around Antarctica.
354 *Science*. 341, 266-270 (2013). <https://doi.org/10.1126/science.1235798>
- 355 46. Tinto, K.J. et al. Ross Ice Shelf response to climate driven by the tectonic imprint on
356 seafloor bathymetry. *Nat. Geosci.* 12, 441–449 (2019). <https://doi.org/10.1038/s41561-019-0370-2>
- 357
- 358 47. Vermeesch, P. Statistical models for point-counting data. *Earth and Planetary Science*
359 *Letters* 501, 112-118 (2018).
- 360 48. Ogg, J. Geomagnetic Polarity Time Scale. In *Geologic Time Scale 2020* (eds. Gradstein, F.
361 M. et al.) 159–192 (Elsevier, 2020).
- 362 49. Rae, J. W. et al. Atmospheric CO₂ over the Past 66 Million Years from Marine Archives.
363 *Annual Review of Earth and Planetary Sciences* 49, 599-631 (2021)
- 364 50. Vermeesch, P. Multi-sample comparison of detrital age distributions. *Chemical*
365 *Geology* 341, 140-146 (2013).

366 **Figure Legends**

367 **Figure 1. Site U1521 location and surrounding geology.** The outcropping regional geology⁴² around
368 the Ross Sea is overlain on the BedMachine Antarctica V1 modern bed topography⁴³. The MEaSURES
369 grounding line, ice sheet margin and basins are used^{44,45} and the map was produced using ArcGIS
370 software. IODP Site U1521 is located on the outer continental shelf of the central Ross Sea. Locations
371 referenced in the text are labelled, including the ANDRILL 2A (AND-2A) and Cape Roberts Project
372 1 (CRP-1) drill sites. The white dashed line indicates the boundary between East and West Antarctic
373 lithosphere⁴⁶. Orange triangles show Cenozoic subglacial volcanic edifices detected based on
374 morphological characteristics, gravity anomalies and magnetic anomalies²⁹. The inset shows an ice-
375 sheet model simulation using a ‘cold’ climate (‘cold’ orbit and a climate with 280 ppm atmospheric
376 CO₂ concentrations) and an estimated Middle Miocene topography⁴. Provenance indicators from Site

377 U1521 Sequence 2 sediments are broadly consistent with an ice sheet similar to or exceeding the extent
378 of this model output.

379 **Figure 2. Selected provenance proxies from IODP Site U1521 compared to Early Miocene**
380 **climate records.** The light blue shaded section (Sequence 2) highlights the interval with sediments
381 of predominantly West Antarctic provenance. The depth of Ross Sea Unconformity (RSU) 4a and 5
382 and seismic surface D-b are indicated in red²³. a) Site U1521 inclination data after 20 mT
383 demagnetisation (red points)²⁶ and polarity interpretation (white = reverse polarity, black = normal
384 polarity, grey = no interpretation). b) Site U1521 lithostratigraphy²⁶. c) Chronostratigraphic
385 sequences. The circled letters between b) and c) mark the depths of the zircon U-Pb samples (Figure
386 3). d) Magnetic susceptibility measured on the whole core²⁶. e) Neodymium isotope signature of the
387 fine fraction. Error bars are 2 S.D. external reproducibility; for provenance interpretations, see
388 Extended Data Figure 4 and references in Supplementary Material. f) Abundance of Eocene-
389 Oligocene dinocysts as a percentage (black) and concentration (i.e., counts per gram sediment; grey).
390 g) Dolerite clast abundance. Errors shown in f) and g) are 95% confidence intervals⁴⁷.
391 Magnetostratigraphic tie points between the polarity interpretations from shipboard data (a)²⁶ and
392 geomagnetic polarity timescale (h)⁴⁸ are marked by purple dashed lines. i) Obliquity sensitivity,
393 indicating the strength of obliquity in the $\delta^{18}\text{O}$ record relative to the theoretical strength of obliquity
394 forcing. This has been interpreted as representing the presence of marine-based Antarctic ice¹⁵. j)
395 Sea-level record based on an oxygen isotope splice². Red and blue shaded intervals indicate
396 pronounced sea-level highstands (>40 m) and lowstands (<-20 m), respectively. MCO = Miocene
397 Climatic Optimum. k) CO₂ reconstruction with a LOESS smoothing (shaded region indicates 1
398 sigma error)⁴⁹. l) Simplified lithological log from the AND-2A record, with diamictites differentiated
399 based on a grounding-zone proximal vs distal glacimarine depositional setting^{11,15}.

400 **Figure 3. Site U1521 detrital zircon U-Pb age distributions.** a) Data displayed as kernel density
401 estimates (KDEs). When present, large Ross Orogeny (~600-500 Ma), Triassic (~240-190 Ma) and
402 Cretaceous (~100 Ma) age peaks are labelled. The age ranges of the Ross Orogeny, Grenville
403 Orogeny and a ~2.7 Ga event recorded in Ross Sea sedimentary strata are illustrated using grey-
404 shaded bars. The sub-bottom depth midpoints of the samples are shown in Figure 2 and listed in the
405 methods section. b) Same data as in a), displayed as a multi-dimensional scaling (MDS) map
406 calculated using the Kolmogorov–Smirnov statistic⁵⁰. Stress (a measurement of the goodness of fit
407 between the disparities and the fitted distances⁵⁰) = 0.072. A MDS plot visualises the degree of
408 similarity between samples, with the proximity of sample points reflecting their similarity. The axis
409 scales are dimensionless and have no physical meaning. The colour of Site U1521 samples (A to I)
410 corresponds their ϵ_{Nd} value. Previously published zircon U-Pb data from Kamb, Whillans and
411 Bindschadler ice streams in West Antarctica, as well as Transantarctic Mountain moraines from
412 inland and coastal regions, are shown in grey^{32,33,34}. The KDEs and region of the MDS plot
413 interpreted as having a West Antarctic provenance are shaded in light blue, consistent with the blue
414 shading in panel a) and Figure 2. Note that although Whillans Ice Stream drains the WAIS, it is
415 excluded from the blue shaded area due to its proximity to the Transantarctic Mountains (Figure 1),
416 resulting in a subglacial sediment provenance signature indistinguishable from East Antarctic
417 detritus³³.

418 **Methods**

419 **Neodymium and Strontium Isotopes**

420 Samples were disaggregated and wet sieved to isolate the <63 μm fraction, which was then dried at
421 60°C. This size fraction represents the bulk composition, as samarium and neodymium are
422 incorporated in equal proportions into most rock-forming minerals, meaning grain-size sorting is not
423 likely to impact results^{51,52}. However, the Rb-Sr system is subject to elemental fractionation during

424 weathering and grain-size sorting, which can influence $^{87}\text{Sr}/^{86}\text{Sr}$ ratios (see ‘Provenance Changes
425 within Sequence 2’ section in Supplementary Material). To remove authigenic Fe-Mn oxyhydroxide
426 phases, samples were leached in a mixture of 0.05 M hydroxylamine hydrochloride, 15% acetic acid,
427 and 0.03 M EDTA at a pH of 4⁵³. A carbonate removal step was not included due to the very low
428 carbonate content²⁶. Leached sediment was dried, homogenised, and 50 mg aliquots were digested on
429 a hotplate in concentrated HF (2 mL), HClO₄ (0.8 mL) and HNO₃ (1 mL) for three to five days, with
430 a subsequent 6 M HCl step. The Nd was isolated from the sample matrix using a cation exchange
431 resin (AG50W-X8, 200-400 µm mesh) and HCl in increasing molarity, followed by a low molarity
432 HCl Ln-Spec resin procedure (50–100 µm mesh). The sample matrix from the cation exchange step
433 was dried down, taken up in HNO₃, then loaded onto Eichrom Sr Spec resin to wash down the matrix
434 and elute the Sr⁵⁴.

435 Neodymium isotopes were measured in the MAGIC laboratories at Imperial College London on a Nu
436 high resolution multi-collector inductively coupled plasma mass spectrometer (HR MC-ICP-MS). To
437 account for instrumental mass bias, isotope ratios were corrected using an exponential law and a
438 $^{146}\text{Nd}/^{144}\text{Nd}$ ratio of 0.7219. Although negligible, interference of ^{144}Sm on ^{144}Nd was corrected for.
439 Bracketing standards were used to correct measured $^{143}\text{Nd}/^{144}\text{Nd}$ ratios to the commonly used JNdi-1
440 value of 0.512115⁵⁵. USGS BCR-2 rock standard was processed alongside all samples and yielded
441 $^{143}\text{Nd}/^{144}\text{Nd}$ ratios consistently within error of the published ratio of 0.512638 ± 0.000015 ⁵⁶. Full
442 procedural blanks for Nd ranged from 7 to 30 pg (n = 6). $^{143}\text{Nd}/^{144}\text{Nd}$ ratios are expressed using
443 epsilon notation (ϵ_{Nd}), which denotes the deviation of a measured ratio from the modern Chondritic
444 Uniform Reservoir (0.512638)⁵⁷ in parts per 10,000.

445 Strontium isotopes were measured in the MAGIC laboratories at Imperial College London on a
446 TIMS (Thermal Ionisation Mass Spectrometer). 10% of the sample was loaded in 1 µL of 6M HCl
447 onto degassed tungsten filaments with 1 µL of TaCl₅ activator. The measured $^{87}\text{Sr}/^{86}\text{Sr}$ ratios were
448 corrected for instrumental mass bias using an exponential law and an $^{88}\text{Sr}/^{86}\text{Sr}$ ratio of 8.375.

449 Interference of ^{87}Rb was corrected for using an $^{87}\text{Rb}/^{85}\text{Rb}$ ratio of 0.386. Analyses of the NIST 987
450 standard reference material were completed every four unknowns, yielding a mean of $0.710290 \pm$
451 0.000041 (2SD, $n = 36$). Samples were corrected to the published value of 0.710252 ± 0.000013 ⁵⁶.
452 The relatively poor reproducibility for our NIST 987 runs was due to technical issues, but is still
453 more than sufficient for interpreting sample results, which change in the 3rd to 4th digit. Accuracy of
454 results was confirmed using rock standard USGS BCR-2, processed with every batch of samples,
455 which yielded $^{87}\text{Sr}/^{86}\text{Sr}$ ratios of 0.705010 ± 0.00029 (2SD, $n = 18$). This is well within error of the
456 published ratio of 0.705013 ± 0.00010 ⁵⁶.

457 **Detrital Zircon U-Pb Dating**

458 The sub-bottom depth midpoints of the nine samples are: A: 220.23, B: 270.03, C: 335.72, D: 373.58, E:
459 410.82, F: 487.40, G: 546.55, H: 588.00 and I: 642.21 mbsf. To ensure there were enough grains for
460 statistical analysis, the above samples were taken over 40 cm intervals. Samples were disaggregated,
461 dried and sieved at 300 μm . Zircons from the <300 μm fraction were concentrated using standard
462 gravity settling and magnetic separation techniques. Samples were then mounted in resin, polished
463 and analysed using an Agilent 7900 laser ablation inductively-coupled plasma mass spectrometer
464 (LA-ICP-MS) with a 25-35 μm pit diameter in the London Geochronology Centre at University
465 College London. Approximately 150 grains resembling zircons were randomly selected for analysis
466 from each sample. Plešovice zircon⁵⁸ was used as a primary standard to correct for instrumental mass
467 bias and depth-dependent inter-element fractionation. Approximate U and Th concentrations were
468 calculated by comparison with NIST 612 glass⁵⁹.

469 Data reduction of the time-resolved mass spectrometer data was performed using GLITTER 4.5⁽⁶⁰⁾.
470 Ages younger than 1100 Ma were calculated using the $^{206}\text{Pb}/^{238}\text{U}$ ratio whilst older grains used the
471 $^{207}\text{Pb}/^{206}\text{Pb}$ ratio. Data were filtered to exclude non-zircons based on zirconium concentrations ($>10^6$
472 counts per second) and a -5/+15% discordance threshold was applied. This yielded at least 92 grains

473 per sample, giving a 95% confidence that any age populations comprising more than 7% of the
474 sample will be measured⁶¹. GJ1 zircon⁶² was used as a secondary standard to verify accuracy of the
475 data. Repeat analyses using zircons with and without existing ablation pits were made to check
476 sample reproducibility; these agreed within the uncertainties associated with random sampling. Final
477 data were processed and visualised using the R package IsoplotR⁶³.

478 **Clast Petrography**

479 The gravel fraction (>2 mm) was characterized in continuum along the core between 648.17 and
480 209.17 mbsf. Clasts exposed in the cut surface of the archive half core were measured, logged and
481 described on the basis of macroscopic features (e.g. shape, colour, texture). Logging aimed to
482 identify the distribution and variation of the gravel-size clasts along the core length. Clast logging
483 followed the methods previously applied to the ANDRILL and Cape Roberts Project drill records
484 from the Ross Sea. On the basis of macroscopic features, clasts were grouped into seven main
485 lithological groups: igneous rocks, quartz fragments, dolerites, volcanic rocks, metamorphic rocks,
486 sedimentary rocks and sedimentary intraclasts^{64,65,66,67}. Data processing involved counting the
487 occurrence of each lithological group over 10 cm core intervals and summarizing this for each core
488 (Extended Data Fig. 3). The total number of clasts was also summed for each metre interval
489 (Extended Data Fig. 3). To highlight the along-core variation in dolerite and volcanic clasts - two of
490 the most indicative lithologies for provenance constraint - the number of these clasts was divided by
491 the total number of clasts in each core (Extended Data Fig. 3). A total of 73 pebble to cobble-sized
492 clasts were sampled for petrographic analysis, of which the most representative of each lithological
493 group were analysed using standard petrographic methods with polarized light microscopy.

494 **Palynology**

495 Sample processing was performed at Utrecht University, following standard techniques of the
496 Laboratory of Palaeobotany and Palynology. Samples were oven-dried and weighed (~15 g dry

497 weight sediment each). One *Lycopodium clavatum* tablet with a known amount of marker spores was
498 added for quantification of palynomorph abundances⁶⁸.

499 Samples were treated with 10% HCl (Hydrochloric acid) and cold 38% HF (Hydrofluoric acid), then
500 sieved over a 10 µm mesh with occasional mild ultrasonic treatment. To avoid any potential
501 processing-related preservation bias, no oxidation or acetolysis was carried out. The processed
502 residue was transferred to microscope slides using glycerine jelly as a mounting medium, and 2
503 slides were analysed per sample at 400× magnification. Slides were examined for detailed marine
504 palynomorphs (dinoflagellate cysts, acritarchs and other aquatic palynomorphs) and, at screening-
505 level, terrestrial palynomorphs (pollen and spore) at Utrecht University. Subsequent detailed analysis
506 of terrestrial palynomorphs on a sub-set of seven samples was undertaken at GNS Science. Of the 23
507 palynological samples analysed for dinocysts, two contained <60 dinocysts (Sequence 1; 594.48
508 mbsf and Sequence 2; 567.75 mbsf) and one was almost barren (yielding only 12 *in situ* dinocysts,
509 Sequence 3A; 374.9 mbsf). The almost barren sample is excluded from all plots. The two low
510 abundance samples are included in our plots but require careful interpretation. Samples between
511 594.48 and 567.75 mbsf and below 594.48 mbsf (cores 65R, 67R, 69R and 71R) were also checked,
512 but yielded few dinocyst specimens. Those present comprised of fragments of mostly reworked
513 dinocysts.

514 Pollen and spore identification followed taxonomic compilations^{69,70}, augmented by key Antarctic
515 literature^{71,72,73}. For pollen and spores, scanning continued until an entire cover slide was completed,
516 or a 100 count reached. Results are presented as specimens/gram, and percentage of all terrestrial
517 palynomorphs. Dinocysts were identified based on a taxonomical index⁷⁴ and informally and
518 formally described species in the literature^{75,76,77,78}. Dinocyst percentages were calculated based on
519 the total *in situ* dinocysts counted, excluding reworked specimens. The percentages of other
520 palynomorph groups such as brackish and freshwater algae (*Cymatiosphaera* spp. and *Pediastrum*
521 spp.) and reworked dinocysts were calculated using the total palynomorphs counted (Fig. 2;

522 Extended Data Fig. 2). *In situ* dinocyst and terrestrial palynomorph absolute abundance (specimens/g
523 dry weight) and the absolute abundance of the other palynomorph groups were calculated by
524 counting the amount of *Lycopodium clavatum* spores encountered, following the equation of
525 Benninghoff (1962)⁷⁹.

526 Protoperidinioid (P) dinocysts are mostly represented by the genera *Brigantedinium*, *Lejeunecysta*,
527 and *Selenopemphix*. Gonyaulacoid (G) dinocysts mostly include *Batiacasphaera* spp.,
528 *Operculodinium* spp. and *Spiniferites* spp. Protoperidinioid cyst percentages (Heterotrophic % in
529 Extended Data Fig. 2) and percentages of the most common species (*Brigantedinium* spp.
530 *Lejeunecysta* spp., *Selenopemphix* spp. and *Selenopemphix antarctica*) were calculated to identify
531 productivity trends and/or the presence of sea ice (see Supplementary Material). P dinocysts are
532 likely produced by heterotrophic dinoflagellates⁸⁰ and, at present, dominate the assemblages in
533 Antarctic sediments in areas with high nutrients and/or (year-round) sea-ice cover. At present,
534 samples in quasi perennial sea-ice covered areas are dominated by *Selenopemphix antarctica*
535 (~75%), with abundant *Brigantedinium* spp. and rare occurrence of other species^{81,82,83}. G cysts are
536 generally produced by phototrophic dinoflagellates. *Operculodinium* spp. is the most abundant, has
537 species representatives among the extant cysts and has been selected to represent temperate-warm
538 conditions. At present, it is almost exclusively found in temperate areas of the Southern Ocean north
539 of the Subantarctic Front and never occurs in circum-Antarctic sediments south of the Polar Front⁸¹.
540 In contrast, it is common to abundant in other Antarctic warm Miocene records^{84,85}. Reworked
541 dinocysts include Eocene and Oligocene taxa (mostly *Vozzhennikovia* spp., but also few *Spinidinium*
542 spp. and *Enneadocysta diktyostila*).

543 **Sediment Volume Estimate**

544 The volume of sediment comprising Sequence 2 was estimated based on seismic data for the Ross
545 Sea continental shelf²³. The isopach maps were developed by interpolating between available seismic

546 reflection profiles²³, giving a total volume of $175,526 \pm 17,553 \text{ km}^3$. The 10% uncertainty accounts
547 for uncertainty in seismic velocities, which vary from 1700-2700 ms^{-1} at Site U1521 based on
548 tomography and 1970-2480 ms^{-1} based on down-hole measurements. As the provenance data suggest
549 a West Antarctic sediment source for Site U1521 Sequence 2, we assume that all the sediments east
550 of 180° and south of 73° are derived from West Antarctica. This is the vast majority ($123,627 \pm$
551 $12,363 \text{ km}^3$) of the sediment across the shelf. Our sediment volume estimate is conservative, as the
552 top of Sequence 2 (surface D-b) has been truncated across much of the continental shelf by RSU4²³.
553 Significant sediment volumes are also likely to be present beyond the edge of the seismic data from
554 the continental rise. Any sediment beneath the modern Ross Ice Shelf is also unaccounted for,
555 although this component is likely to be small.

556 To translate this sediment volume into an erosion rate, the approach and uncertainty range of Paxman
557 et al. (2019)¹⁸ was used to account for porosity and a small biogenic sediment component (Extended
558 Data Table 2). We note that using generic values in our porosity calculation is crude, with variation
559 in the porosity of these Antarctic sediments likely to be significant⁸⁶, but nevertheless sufficient for
560 our order-of-magnitude estimate of erosion. It is reasonable to assume the major ice divides have
561 remained in largely the same positions since the Early Miocene, as indicated by various modelling
562 studies using reconstructed topographies^{4,5,16}. The size of the eastern Ross Sea catchment (i.e. Ross
563 Sea sector of the WAIS) was therefore assumed to be similar to the modern, with a 20% uncertainty.
564 Some sediment in these units clearly contains reworked material; there are high concentrations of
565 Eocene-Oligocene palynomorphs and diatoms. Although this means our erosion rate is not indicative
566 of pure bedrock incision, it still represents a significant change to the topography and bathymetry of
567 West Antarctica. The material removed likely exceeds our conservative estimate of $\sim 87 \text{ m}$ across the
568 catchment. The 317,416 year duration is based on the cyclostratigraphic analyses described in the
569 age model section, with a 20,000 year uncertainty.

570 **IODP Site U1521 Age Model**

571 The age model for IODP Site U1521 uses magnetostratigraphy, biostratigraphy, cyclostratigraphy,
572 $^{87}\text{Sr}/^{86}\text{Sr}$ dating of microfossils, and $^{40}\text{Ar}/^{39}\text{Ar}$ ages of hornblende grains to correlate rock units to the
573 Geomagnetic Polarity Timescale (GPTS)⁴⁸. Key events and tie points are summarized in Extended
574 Data Table 1 and illustrated in Extended Data Figures 1 and 8. Biostratigraphic constraints include
575 first and last appearance datums of diatoms. The maximum and minimum age range reported for
576 these datums are derived from total and average ranges^{87,88} and hybrid range models derived from
577 Constrained Optimization (CONOP) methods^{88,89}. Hybrid range model ages are used as primary
578 constraints for our age model. This is because they best account for up section reworking of
579 microfossil datums, which is common in glacial sedimentary environments, whilst recognising that
580 major down section reworking is unlikely (partly because of the rarity of bioturbated intervals). They
581 are marked by base of arrows in Extended Data Figure 1 and mentioned in the text below.

582 Biostratigraphic datums and magnetic polarity reversals provide tie points to construct lines of
583 correlation (LOC) with the GPTS. The age model presented here includes the interval of West
584 Antarctic sediment provenance (Sequence 2) and is described from the base of the borehole at 650
585 mbsf to 75 mbsf.

586 Biostratigraphic constraints through the interval from 650 mbsf to near the top of Sequence 3B (at
587 ~286.1 mbsf) are sparse as the sediments are deeper than the Opal-CT transition and diatom
588 preservation is relatively poor. Our correlation of the four distinct magnetozones R5, N4, R4, and N3
589 to the GPTS is therefore primarily based on regional correlation of prominent seismic reflectors to
590 other dated drill cores from the Ross Sea shelf, backed up by diatom biostratigraphic constraints. The
591 section from 650 mbsf to 567.95 mbsf at Site U1521 (Sequence 1) is characterised by reversed
592 magnetic polarity but offers no constraints which we can confidently use for correlating this reversed
593 interval to the GPTS. However, robust age constraint for sediments at the base of Sequence 2 can be
594 determined through regional correlation of RSU5 to other sites where chronostratigraphic data are
595 available. RSU5 intersects Site U1521 at 567.95 mbsf (the base of Sequence 2) and is correlated

596 across the Glomar Challenger Basin and tied to DSDP Site 273 at 282 mbsf²³. The LAD of *T.*
597 *praeфрага* is observed at 309 mbsf in DSDP Site 273, which suggests that RSU5 is younger than
598 17.95 Ma at that site. RSU5 cannot be directly correlated into the western Ross Sea, but a major
599 unconformity (U2) occurs in the AND-2A drill site at 774.94 mbsf and likely corresponds with
600 RSU5 based on chronostratigraphy¹¹. Specifically, sediments that directly underlie U2 in AND-2A
601 are characterised by a reversed magnetic polarity and are correlated to Chron C5Er (18.636 to 18.497
602 Ma) based on constraints that include ⁴⁰Ar/³⁹Ar dates of 18.82 ± 0.15 Ma on pumice clasts within a
603 tuffaceous siltstone at 831.66 mbsf. The age of sediments that overlie U2 at the AND-2A drill site
604 are constrained by the FAD of *T. praeфрага* at 771.5 mbsf (<18.46 to 18.58 Ma), and a ⁴⁰Ar/³⁹Ar date
605 of 18.04 ± 0.31 Ma on pumice clasts within a tuffaceous siltstone at 709.17 mbsf. These observations
606 require correlation of the reversed magnetic polarity zone that characterise the sediments above U2
607 to Chron C5Dr.2r (18.007 to 17.676 Ma). All evidence presented above shows that between ~18.6
608 and ~17.8 Ma, a significant, regionally extensive, erosional event (or series of events) created surface
609 RSU5/U2.

610 Sediments deposited on top of RSU5 at Site U1521 are characterised by reversed magnetic polarity.
611 Based on the known age of RSU5 at DSDP Site 273 and U2 at AND-2A, we correlate the top of
612 reversed magnetozone R5 in Site U1521 to Chron C5Dr.2r. This interpretation is consistent with the
613 observation that *T. praeфрага* is not present in a diatom-bearing sample at 563 mbsf, despite
614 comprehensive searches for this species in this sample as well as diatom-bearing samples higher in
615 Sequence 2. As *T. praeфрага* is a small and compact diatom not prone to fragmentation which would
616 likely be preserved in the observed diatom assemblages, we are confident this absence is not a result
617 of poor preservation below the Opal-CT transition. *T. praeфрага* is a common species in upper
618 Oligocene and lower Miocene sediments recovered from several sites across the Ross Sea, including
619 Cape Roberts Project-2/2A, DSDP Site 273, and AND-2A^{11,90,91}. The total reported CONOP model
620 based age range for the LAD of *T. praeфрага* is 17.95 to 16.82 Ma and the hybrid model range is

621 17.95 to 17.36 Ma^{87,88,89}. Consequently, we view the absence of *T. praeфрага* as strong evidence that
622 the sediments above 563 mbsf at Site U1521 are younger than 17.95 Ma.

623 We then correlate the magnetic polarity reversal (MPR) R5/N5 between 526.8 and 524 mbsf to
624 C5Dr.1n/C5Dr.2r (17.676 Ma), the MPR N4/R4 between 517.2 and 515.1 mbsf to C5Dr.1r/C5Dr.1n
625 (17.634 Ma), and the MPR R4/N3 between 400.5 and 397.2 mbsf to C5Dn/C5Dr.1r (17.466 Ma). We
626 extend a line of correlation from this MPR to the top of Sequence 2, where it intersects with seismic
627 surface D-b²³. The correlation presented here by interpolating through these MPRs indicates
628 sediments in Sequence 2 span the time interval from ~17.7-17.4 Ma. The occurrence of the diatom
629 taxon *Thalassiosira* sp. cf. *T. bukryi* at 450.52 mbsf supports this correlation as the range reported for
630 this taxon at ODP Site 744 is 17.7-17.4 Ma^{88,92}.

631 To refine the likely sedimentation rate and timespan of Sequence 2, a cyclostratigraphic analysis was
632 conducted on clast abundance data (Extended Data Fig. 3) spanning 568 to 380 mbsf. These data
633 were analysed using TimeOpt⁹³, which is a statistical optimization method for astronomical time
634 scale construction and astrochronologic testing, executed by the *astrochron* package in R⁹⁴ (function
635 ‘timeOpt’). Given a range of plausible sedimentation rates and a series of specified astronomical
636 periodicities (for precession, obliquity, and eccentricity), TimeOpt identifies the age model that
637 results in a time-series that best aligns with the predictions of Milankovitch theory. Specifically, two
638 diagnostic attributes of the astronomical hypothesis are evaluated: the hierarchy of cyclic frequencies
639 expected of Milankovitch Cycles, r^2_{spectral} , and the match between eccentricity cycles and the
640 precession-band envelope, r^2_{envelope} ^{93,95}. These two values (r^2_{power} and r^2_{envelope}) are multiplied to
641 produce an r^2_{opt} value, which provides insight into the strength of a hypothesized astronomical signal
642 at each evaluated sedimentation rate.

643 Assuming plausible average sedimentation rates between 40 cm kyr⁻¹ and 65 cm kyr⁻¹, TimeOpt
644 yields an optimal sedimentation rate of 59.2 cm kyr⁻¹ for Sequence 2, with an r^2_{opt} of 0.396. To assess

645 the statistical significance of the result, a Monte Carlo astrochronologic test is conducted to evaluate
646 the null hypothesis that the observed variability in clast abundance arises entirely by stochastic
647 processes, rather than astronomical forcing. The Monte Carlo simulations are generated using the
648 function “timeOptSim”, which creates a large number of similar time-series of stochastic (“red”)
649 noise, to assess the probability that such datasets can produce an r^2_{opt} value comparable to the one
650 generated by the clast abundance data^{93,95}. This analysis yields a p-value of 0.005, indicating that the
651 null hypothesis (i.e. the data is generated from a stochastic “red noise” process; specifically an AR1
652 process) can be rejected with a high degree of confidence. Given that the astrochronologically-
653 estimated sedimentation rate is derived independently from the paleomagnetic data, their consistency
654 is remarkable and provides strong evidence in support of an estimated duration of ~317 kyrs for
655 Sequence 2 (Extended Data Fig. 1)²⁶.

656 While the ‘floating’ TimeOpt-derived astronomical time scale preserves information about elapsed
657 time, it must be separately anchored to a specific numerical age. To do so, we use the ‘slideCor’
658 function in the *astrochron* package⁹⁴; this is an automated approach to find the optimal anchoring of
659 the floating TimeOpt-derived time scale to the theoretical astronomical solution of Laskar et al.
660 (2004)⁹⁶. Specifically, we have applied a Taner bandpass filter⁹⁷, isolating the periods between 60 ka
661 and 27 ka for both the obliquity component of the astronomical solution⁹⁶, and for the TimeOpt-
662 derived floating astrochronology. The optimal match between the astronomical solution and floating
663 astrochronology is identified using the squared Pearson correlation coefficient.

664 Independent biostratigraphic and magnetostratigraphic constraints mean we can restrict our
665 ‘slideCor’ assessment to a feasible ~800 ka interval; our lower limit (17.950 Ma) is based on the
666 absence of *T. praefraga* and the correlations of RSU5 described above, and our upper limit is based
667 on the C5Cr/C5Dn MPR (17.154 Ma). Since the precise relationship between clast abundance and
668 astronomical forcing is not known with certainty, any time-anchor for the astronomically calibrated
669 section should be treated as having an uncertainty of at least a full obliquity cycle (~41 ka).

670 Application of the slideCor function identifies two plausible regions of the astronomical solution for
671 anchoring the Sequence 2 clast abundance data. The optimal match ($r^2 = 0.8497$) results in an
672 astronomically calibrated section ranging from 17.601 Ma to 17.918 Ma (± 0.02 Ma). This would
673 indicate that the interval is ~ 140 -220 kyrs older than the age range suggested by the paleomagnetic
674 interpretation, giving a very poor match with the measured polarities. However, a slightly less
675 optimal match ($r^2 = 0.7704$) anchors the section to span 17.398 Ma to 17.715 Ma (± 0.02 Ma), which
676 places it within ~ 40 kyrs of the paleomagnetic interpretation. This agreement of geochronological
677 frameworks derived from paleomagnetism and astrochronology, which are broadly independent,
678 provides strong support for the age model presented here.

679 Uncertainties in the magnetostratigraphic age model, most notably for Subchrons C5Dr.1n and
680 C5Dr.1r and Chron C5Dn, may account for some of the slight disagreement with the
681 astrochronological approach described above. The available astronomically tuned durations of these
682 (sub-)chrons agree within 10%^{98,99}. The small discrepancies in duration of (sub-)chrons originate
683 from the astronomical tuning approach (carbon and oxygen isotopes tuned to eccentricity, tilt and
684 precession at Site 1090⁽⁹⁸⁾ and carbonate content to eccentricity only at Site U1336⁽⁹⁹⁾), as well as
685 physical and palaeomagnetic recording processes such as bioturbation and the palaeomagnetic lock-
686 in depth^{100,101}. Paleomagnetic measurement methods are discussed in detail in the cruise report²⁶.

687 We suggest 17.95-17.40 Ma as the absolute uncertainty of the timing of Sequence 2 deposition,
688 based on the absence of *T. praefraga* (17.95 Ma) and occurrence of MPR C5Dn/C5Dr.1r (17.466
689 Ma) near the top of Sequence 2. However, more precise constraint on the duration of Sequence 2
690 deposition can be achieved based on the remarkable agreement of sedimentation rates based on the
691 astronomical analysis of clast data and interpolation through magnetostratigraphic tie points, which
692 suggest deposition occurred over ~ 317 kyrs. Combined with the close correlation between our
693 astrochronological analyses and the timing of MPRs, we suggest a more precise interval for the
694 deposition of Sequence 2, spanning ~ 17.72 -17.40 ± 0.02 Ma. The ~ 20 kyr error represents

695 uncertainty in the phase relationship between clast abundance and obliquity forcing. This range
696 coincides closely with many independent records indicating ice-sheet growth, including a sea-level
697 lowstand recorded on the New Jersey continental margin (~17.8-17.46 Ma)¹, evidence for ice sheet
698 growth in the AND-2A drill core sediments (~17.8-17.4 Ma)¹¹ and a peak in obliquity sensitivity
699 (~17.8-17.5 Ma)¹⁵ (Fig. 2).

700 The age of Sequence 3A and 3B (324.20- 209.17 mbsf), bracketed by seismic surface D-b and
701 regional unconformity RSU4a, is difficult to tightly constrain. Diatom preservation increases
702 significantly in a sample at 286.1 mbsf at the base of Sequence 4A and the FADs of *Nitzschia sp. 17*
703 *Schrader*, *Synedropsis cheethamii*, and *Denticulopsis maccollumii* suggest sediments below this
704 stratigraphic level are older than 17 Ma. The LAD of *F. maleinterpretaria* in this sample provides a
705 minimum age constraint and suggests that the sediments below 286.1 Ma must be older than 16.41
706 Ma. These constraints require that the sediments between 344.6 and 286.3 mbsf, characterised by
707 reversed polarity, correlate with either the Subchron C5Cn.2r or the base of Chron C5Cr. Correlation
708 to the base of Chron C5Cr is our favoured option as this would indicate that the interval of time
709 missing across seismic surface D-b is relatively short, whereas regional unconformity RSU4a at the
710 top of this unit records a hiatus of longer duration. The alternative interpretation is shown with a
711 dashed line in Extended Data Figure 1.

712 We constrain the slope of the LOC through Sequence 3B based on the sedimentation rate indicated
713 for the diatom-bearing Sequence 4B as the sediments are similar, although affected by diagenesis in
714 Sequence 3B. The sedimentation rate in Sequence 3A is assumed to be comparable to the Sequence 2
715 diamicts. We also acknowledge that the actual first appearance of the diatom taxa identified in the
716 sample at 286.1 mbsf may have originally been deeper, but their presence has since been obscured by
717 diagenesis. This would require that the LOC sit to the left (younger) of its current position.
718 Therefore, we include an error box (orange box in Extended Data Fig. 1) in our age model to show

719 that the LOC could occur anywhere within this area depending on the amount of time missing across
720 D-b and the sedimentation rate during deposition. We are confident that the MPR between 400.5 and
721 397.2 mbsf (N3/R3) is C5Dn/C5Dr.1r (17.466 Ma) based on constraints above and below this
722 interval outlined above and place our LOC through the reversal. This LOC requires a time gap of ~
723 180 kyrs across regional seismic surface D-b²³ that separates Sequences 2 and 3.

724 The relatively thin interval of reversed polarity within Chron C5Dn (at ca. 380 mbsf) is not identified
725 in the current version of the GPTS (Extended Data Fig. 8), but a similar short-duration reversed
726 polarity event roughly halfway through Chron C5Dn is recorded in the AND-2A
727 magnetostratigraphic record¹¹. Taking the palaeomagnetic uncertainties of ice-proximal sediments
728 into account, we hypothesise that this rarely recorded reversed polarity event could be a genuine
729 feature of the geomagnetic field that has not been detected in marine sediments due to signal
730 smoothing at low sedimentation rates¹⁰².

731 The age of sediments above RSU4a are very well constrained by diatom data, ⁸⁷Sr/⁸⁶Sr ages and
732 magnetostratigraphy. The LAD of *F. maleinterpretaria* indicates that the sediments above 286.1
733 mbsf must be younger than 16.41 Ma. An ⁸⁷Sr/⁸⁶Sr date on shell fragments at 272.65 mbsf indicates
734 the interval with reversed polarity containing the fragments correlates with Subchron C5Cn.1r
735 (16.351 to 16.261 Ma). This correlation means that the hybrid age model underestimates the
736 maximum age of the FAD of *Nitzschia grossepunctata*, which occurs at 286.1 mbsf, and suggests the
737 age indicated by the total range model age for this datum (16.23 Ma) is more likely. Together, these
738 data indicate that the base of Sequence 4A dates to less than ~16.351 Ma. We correlate the MPR
739 (R3/N2) between 209 and 205 mbsf to C5Cn.1n/C5Cn.1r (16.261 Ma). The sequence of well-dated
740 shells through Sequence 4B allows us to correlate the sediments between 209 and 106.3 mbsf that are
741 characterised by normal polarity with Subchron C5Cn.1n (16.261 to 15.994 Ma) and the MPR
742 between 106.3 and 105.5 to C5Br/C5Cn.1n (15.994 Ma). The FADs of *Denticulopsis lauta*,
743 *Actinocyclus ingens*, *Denticulopsis hyalina*, and *Denticulopsis simonsenii* at 84.99 mbsf indicate a

744 major hiatus at this depth spanning from ~15.83 Ma to at least 14.48 Ma. This stratigraphic horizon
745 correlates with RSU4, a major regional unconformity²³.

746 **Sediment Provenance Interpretations**

747 To interpret the provenance data from IODP Site U1521, they must be placed in a regional context. In
748 the Supplementary Material, we therefore present a short geological summary of the Ross Sea
749 sector^{31,37,103-169}, including a compilation of published zircon U-Pb data^{33,104-128}. We also include a
750 more detailed discussion of our hornblende ⁴⁰Ar/³⁹Ar^{135,153,170-174}, clast petrography, clay
751 mineralogy^{157,182-187}, and palynology^{35,71,77,83,188-191} datasets. Additional insights into the sediment
752 provenance of Sequences 1, 2 and 3A are also explored^{23,33,38,183,192-198}. A compilation of literature
753 neodymium and strontium isotope data (visualised in Extended Data Figures 4 and 5) is provided in
754 Supplementary Table 1.

755 **Additional References**

- 756 51. Goldstein, S. L., & Hemming, S. R. Long-lived isotopic tracers in oceanography,
757 paleoceanography, and ice-sheet dynamics. *Treatise on geochemistry* 6, 625 (2003).
- 758 52. Garçon, M., Chauvel, C., France-Lanord, C., Huyghe, P., & Lavé, J. (2013). Continental
759 sedimentary processes decouple Nd and Hf isotopes. *Geochimica et Cosmochimica*
760 *Acta*, 121, 177-195.
- 761 53. Gutjahr, M., Frank, M., Stirling, C. H., Klemm, V., Van de Flierdt, T., & Halliday, A. N.
762 Reliable extraction of a deepwater trace metal isotope signal from Fe–Mn oxyhydroxide
763 coatings of marine sediments. *Chemical Geology* 242, 351-370 (2007).
- 764 54. Simões Pereira, P. et al. Geochemical fingerprints of glacially eroded bedrock from West
765 Antarctica: Detrital thermochronology, radiogenic isotope systematics and trace element
766 geochemistry in Late Holocene glacial-marine sediments. *Earth-Science Reviews* 182, 204-
767 232 (2018).
- 768 55. Tanaka, T. et al. JNdi-1: a neodymium isotopic reference in consistency with LaJolla
769 neodymium. *Chem. Geol.* 168, 279–281 (2000).
- 770 56. Weis, D. et al. High-precision isotopic characterization of USGS reference materials by
771 TIMS and MC-ICP-MS. *Geochem. Geophys. Geosyst.* 7, Q08006 (2006).
- 772 57. Jacobsen, S. B. & Wasserburg, G. J. *Earth planet. Sci. Lett.* 50, 139 (1980).
- 773 58. Sláma, J. et al. Plešovice zircon—a new natural reference material for U–Pb and Hf
774 isotopic microanalysis. *Chemical Geology* 249, 1-35 (2008).

- 775 59. Pearce, N. J. et al. A compilation of new and published major and trace element data for
776 NIST SRM 610 and NIST SRM 612 glass reference materials. *Geostandards newsletter* 21,
777 115-144 (1997).
- 778 60. Griffin, W. L. GLITTER: data reduction software for laser ablation ICP-MS. *Laser*
779 *Ablation ICP-MS in the Earth Sciences: Current practices and outstanding issues*, 308-311
780 (2008).
- 781 61. Vermeesch, P. How many grains are needed for a provenance study? *Earth and Planetary*
782 *Science Letters* 224, 441-451 (2004).
- 783 62. Jackson, S. E., Pearson, N. J., Griffin, W. L., & Belousova, E. A. The application of laser
784 ablation-inductively coupled plasma-mass spectrometry to in situ U–Pb zircon
785 geochronology. *Chemical geology* 211, 47-69 (2004).
- 786 63. Vermeesch, P. IsoplotR: A free and open toolbox for geochronology. *Geoscience*
787 *Frontiers* 9, 1479-1493 (2018).
- 788 64. Talarico F. & Sandroni S. Petrography, Mineral Chemistry and Provenance of Basement
789 Clasts in the CRP-1 Drillcore (Victoria Land Basin, Antarctica). *Terra Antarctica* 5, 601-610
790 (1998).
- 791 65. Talarico, F., Sandroni, S., Provenance signature of the Antarctic Ice Sheets in the Ross
792 Embayment during the Late Miocene to Early Pliocene: the ANDRILL AND-1B core
793 record. *Global and Planetary Change* 69, 103–123 (2009).
- 794 66. Talarico F., Sandroni S., Fielding C.R. & Atkins C. Variability, Petrography and
795 Provenance of Basement Clasts from CRP-2/2A Drillcore (Victoria Land Basin, Ross Sea,
796 Antarctica). *Terra Antarctica* 7, 529-544 (2000).
- 797 67. Sandroni, S., and Talarico, F. M. Petrography and provenance of basement clasts and clast
798 variability in CRP-3 drillcore (Victoria Land Basin, Antarctica), *Terra Antarctica* 8, 449-
799 467 (2001).
- 800 68. Wood, G. D., Gabriel, A. M. & Lawson, J. C. In: *Palynology: Principles and Applications*
801 (Eds Jansonius, J. & McGregor, D. C.) 29–50. American Association of Stratigraphic
802 Palynologists Foundation, Dallas, TX (1996).
- 803 69. Raine, J.I., Mildenhall, D.C., Kennedy, E.M. New Zealand fossil spores and pollen: an
804 illustrated catalogue. In: *GNS Science Miscellaneous Series No. 4*, 4th edition.
805 <http://data.gns.cri.nz/sporepollen/index.htm> (2011).
- 806 70. Prebble, J. G. Descriptions and occurrences of pollen and spores from New Zealand
807 Cenozoic sediments, *GNS Science Internal Report 2016/09*, 137 (2016).
- 808 71. Askin, R.A. Spores and pollen from the McMurdo Sound erratics, Antarctica In:
809 *Palaeobiology and Palaeoenvironments of Eocene Rocks, McMurdo Sound, East*
810 *Antarctica. Antarctic Research Series v76* (Eds. Stilwel, J.D. and Feldman, R.M.),
811 American Geophysical Union 2000 (2000).
- 812 72. Askin, R.A. and Raine, J. I. Oligocene and Early Miocene terrestrial palynology of the
813 Cape Roberts Drillhole CRP-2/2A, Victoria Land Basin, Antarctica. *Terra Antarctica* 7,
814 493-501 (2000).
- 815 73. Truswell, E.M. Recycled Cretaceous and Tertiary pollen and spores in Antarctic marine
816 sediments: a catalogue. *Palaeontographica Abteilung B* 186, 121-174 (1983).

- 817 74. Fensome, R. A. & Williams, G. L. The Lentin and Williams index of fossil dinoflagellates.
818 American Association of Stratigraphic Palynologists Foundation Contribution Series 42
819 (2004).
- 820 75. Hannah, M. J., Wilson, G. J. & Wrenn, J. H. Oligocene and miocene marine palynomorphs
821 from CRP-2/2A, Victoria Land Basin, Antarctica. *Terra Antarct.* 7 503–511 (2000).
- 822 76. Hannah, M. J. The palynology of ODP site 1165, Prydz Bay, East Antarctica: a record of
823 Miocene glacial advance and retreat. *Palaeogeogr. Palaeoclimatol. Palaeoecol.* 231, 120–
824 133 (2006).
- 825 77. Clowes, C. D., Hannah, M. J., Wilson, G. J. & Wrenn, J. H. Marine palynostratigraphy of
826 the Cape Roberts Drill-holes, Victoria Land Basin, Antarctica, with descriptions of six new
827 species of organic-walled dinoflagellate cyst. *Mar. Micropaleontol.* 126, 65–84 (2016).
- 828 78. Bijl P., et al. Stratigraphic calibration of Oligocene–Miocene organic-walled dinoflagellate
829 cysts from offshore Wilkes Land, East Antarctica, and a zonation proposal. *J.*
830 *Micropalaeontology* 37, 105–138 (2018). <https://doi.org/10.5194/jm-37-105-2018>
- 831 79. Benninghoff, W. S. Calculation of pollen and spores density in sediments by addition of
832 exotic pollen in known quantities. *Pollen et Spores* 6, 332–333 (1962).
- 833 80. Harland, R., & Pudsey, C. J. Dinoflagellate cysts from sediment traps deployed in the
834 Bellingshausen, Weddell and Scotia seas, Antarctica. *Mar. Micropaleontol.* 37, 77-99
835 (1999).
- 836 81. Prebble, J. G. et al. An expanded modern dinoflagellate cyst dataset for the Southwest
837 Pacific and Southern Hemisphere with environmental associations. *Mar. Micropaleontol.*
838 101, 33–48 (2013).
- 839 82. Hartman, J. D., Bijl, P. K., & Sangiorgi, F. A review of the ecological affinities of marine
840 organic microfossils from a Holocene record offshore of Adélie Land (East
841 Antarctica). *Journal of Micropalaeontology* 37, 445-497 (2018).
- 842 83. Zonneveld, K. A. et al. Atlas of modern dinoflagellate cyst distribution based on 2405 data
843 points. *Review of Palaeobotany and Palynology* 191, 1-197 (2013).
- 844 84. Warny, S. et al. Palynomorphs from a sediment core reveal a sudden remarkably warm
845 Antarctica during the middle Miocene. *Geology* 37, 955–958 (2009).
- 846 85. Sangiorgi, F., et al. Southern Ocean warming and Wilkes Land ice sheet retreat during the
847 mid-Miocene. *Nature Communications* 9, 1-11 (2018).
- 848 86. Niessen, F., Gebhardt, A. C., Kuhn, G., Magens, D., & Monien, D. Porosity and density of
849 the AND-1B sediment core, McMurdo Sound region, Antarctica: Field consolidation
850 enhanced by grounded ice. *Geosphere* 9, 489-509 (2013).
- 851 87. Cody, R. D., Levy, R. H., Harwood, D. M., & Sadler, P. M. Thinking outside the zone:
852 high-resolution quantitative diatom biochronology for the Antarctic Neogene. *Palaeogeog.*
853 *Palaeoclimatol. Palaeoecol.* 260, 92-121 (2008).
- 854 88. Florindo, F. et al. Paleomagnetism and biostratigraphy of sediments from Southern Ocean
855 ODP Site 744 (southern Kerguelen Plateau): implications for early-to-middle Miocene
856 climate in Antarctica. *Global and Planetary Change* 110, 434–454 (2013).
- 857 89. Crampton, J. S. et al. Southern Ocean phytoplankton turnover in response to stepwise
858 Antarctic cooling over the past 15 million years. *Proc. Natl Acad. Sci. USA* 113, 6868–
859 6873 (2016).

- 860 90. Scherer, R., Bohaty, S. M., & Harwood, D. M. Oligocene and lower Miocene siliceous
861 microfossil biostratigraphy of Cape Roberts Project Core CRP-2/2A, Victoria Land Basin,
862 Antarctica. *Terra Antarctica* 7, 417-442. (2000).
- 863 91. Taviani, M. et al. Palaeontological characterisation and analysis of the AND-2A core,
864 ANDRILL Southern McMurdo Sound Project, Antarctica. *Terra Antarctica* 15, 113-146
865 (2008).
- 866 92. Farmer, R.K. (2011). The application of biostratigraphy and paleoecology at Southern
867 Ocean drill sites to resolve early to middle Miocene paleoclimatic events [M.S. thesis].
868 University of Nebraska-Lincoln.
- 869 93. Meyers, S. R. The evaluation of eccentricity-related amplitude modulation and bundling in
870 paleoclimate data: An inverse approach for astrochronologic testing and time scale
871 optimization. *Paleoceanography* 30, 1625-1640 (2015).
- 872 94. Meyers, S.R. *astrochron: An R Package for Astrochronology* (2014).
873 <http://cran.rproject.org/package=astrochron>
- 874 95. Meyers, S. R. Cyclostratigraphy and the problem of astrochronologic testing. *Earth-Science*
875 *Reviews* 190, 190-223 (2019).
- 876 96. Laskar, J. et al. (2004). A long-term numerical solution for the insolation quantities of the
877 Earth. *Astronomy & Astrophysics* 428, 261-285.
- 878 97. Taner, M. T. *Attributes Revisited*. Technical Report. Rock Solid Images, Inc. (1992).
- 879 98. Billups et al. Astronomic calibration of the late Oligocene through early Miocene
880 geomagnetic polarity time scale, *Earth and Planetary Science Letters* 224, 33-44 (2004).
881 doi:10.1016/j.epsl.2004.05.004
- 882 99. Kochhann, K.G. et al. Eccentricity pacing of eastern equatorial Pacific carbonate
883 dissolution cycles during the Miocene Climatic Optimum. *Paleoceanography* 31, 1-17
884 (2016). doi: 10.1002/2016PA002988
- 885 100. Suganuma, Y. et al. 10Be evidence for delayed acquisition of remanent magnetization in
886 marine sediments: Implication for a new age for the Matuyama–Brunhes boundary. *Earth*
887 *and Planetary Science Letters* 296, 443-450 (2010). doi:10.1016/j.epsl.2010.05.031
- 888 101. Suganuma, Y. et al. Post-depositional remanent magnetization lock-in for marine sediments
889 deduced from 10Be and paleomagnetic records through the Matuyama–Brunhes boundary.
890 *Earth and Planetary Science Letters* 311, 39-52 (2011). doi: 10.1016/j.epsl.2011.08.038
- 891 102. Roberts, A.P. & Winklhofer, M. Why are geomagnetic excursions not always recorded in
892 sediments? Constraints from post-depositional remanent magnetization lock-in modelling.
893 *Earth and Planetary Science Letters* 227, 345-359 (2004). doi: 10.1016/j.epsl.2004.07.040
- 894 103. Boger, S. D. Antarctica—before and after Gondwana. *Gondwana Research* 19, 335-371
895 (2011).
- 896 104. Siddoway, C. S. Tectonics of the West Antarctic Rift System: new light on the history and
897 dynamics of distributed intracontinental extension. In: Cooper, A., Raymond, C. and the
898 10th ISAES Editorial Team (Eds.) *Antarctica: A Keystone in a Changing World*, 91-114.
899 The National Academic Press, USA (2008).
- 900 105. Mukasa, S. B., & Dalziel, I. W. Marie Byrd Land, West Antarctica: Evolution of
901 Gondwana's Pacific margin constrained by zircon U-Pb geochronology and feldspar
902 common-Pb isotopic compositions. *Geological Society of America Bulletin* 112, 611-627
903 (2000).

- 904 106. Weaver, S. D., Adams, C. J., Pankhurst, R. J., & Gibson, I. L. Granites of Edward VII
905 Peninsula, Marie Byrd Land: anorogenic magmatism related to Antarctic-New Zealand
906 rifting. *Earth and Environmental Science Transactions of The Royal Society of*
907 *Edinburgh* 83, 281-290 (1992).
- 908 107. Korhonen, F. J., Saito, S., Brown, M., Siddoway, C. S., & Day, J. M. D. Multiple
909 generations of granite in the Fosdick Mountains, Marie Byrd Land, West Antarctica:
910 implications for polyphase intracrustal differentiation in a continental margin
911 setting. *Journal of Petrology* 51, 627-670 (2010).
- 912 108. Craddock, J. et al. Precise U-Pb zircon ages and geochemistry of Jurassic granites,
913 Ellsworth-Whitmore terrane, central Antarctica. *GSA Bulletin* 129, 118-136 (2017).
- 914 109. Pankhurst, R. J., Weaver, S. D., Bradshaw, J. D., Storey, B. C., & Ireland, T. R.
915 Geochronology and geochemistry of pre-Jurassic superterrane in Marie Byrd Land,
916 Antarctica. *Journal of Geophysical Research: Solid Earth* 103, 2529-2547 (1998).
- 917 110. Flowerdew, M. J. et al. Combined U-Pb geochronology and Hf isotope geochemistry of
918 detrital zircons from early Paleozoic sedimentary rocks, Ellsworth-Whitmore Mountains
919 block, Antarctica. *Geological Society of America Bulletin* 119, 275-288 (2007).
- 920 111. Elliot, D. H., & Fanning, C. M. Detrital zircons from upper Permian and lower Triassic
921 Victoria Group sandstones, Shackleton Glacier region, Antarctica: evidence for multiple
922 sources along the Gondwana plate margin. *Gondwana Research* 13, 259-274 (2008).
- 923 112. Elliot, D. H., Fanning, C. M., & Hulett, S. R. Age provinces in the Antarctic craton:
924 Evidence from detrital zircons in Permian strata from the Beardmore Glacier region,
925 Antarctica. *Gondwana Research* 28, 152-164 (2015).
- 926 113. Goodge, J. W., Williams, I. S., & Myrow, P. Provenance of Neoproterozoic and lower
927 Paleozoic siliciclastic rocks of the central Ross orogen, Antarctica: Detrital record of rift-,
928 passive-, and active-margin sedimentation. *Geological Society of America Bulletin* 116,
929 1253-1279 (2004).
- 930 114. Paulsen, T. S. et al. Detrital mineral ages from the Ross Supergroup, Antarctica:
931 Implications for the Queen Maud terrane and outboard sediment provenance on the
932 Gondwana margin. *Gondwana Research* 27, 377-391 (2015).
- 933 115. Paulsen, T. S. et al. Correlation and Late-Stage Deformation of Liv Group Volcanics in the
934 Ross-Delamerian Orogen, Antarctica, from New U-Pb Ages. *The Journal of Geology* 126,
935 307-323 (2018).
- 936 116. Goodge, J. W., Fanning, C. M., Norman, M. D., & Bennett, V. C. Temporal, isotopic and
937 spatial relations of early Paleozoic Gondwana-margin arc magmatism, central
938 Transantarctic Mountains, Antarctica. *Journal of Petrology* 53, 2027-2065 (2012).
- 939 117. Paulsen, T. S. et al. Age and significance of 'outboard' high-grade metamorphics and
940 intrusives of the Ross orogen, Antarctica. *Gondwana Research* 24, 349-358 (2013).
- 941 118. Rowell, A. J. et al. An active Neoproterozoic margin: evidence from the Skelton Glacier
942 area, Transantarctic Mountains. *Journal of the Geological Society* 150, 677-682 (1993).
- 943 119. Encarnación, J., & Grunow, A. Changing magmatic and tectonic styles along the paleo-
944 Pacific margin of Gondwana and the onset of early Paleozoic magmatism in
945 Antarctica. *Tectonics* 15, 1325-1341 (1996).
- 946 120. Goodge, J. W., Hansen, V. L., Peacock, S. M., Smith, B. K., & Walker, N. W. Kinematic
947 evolution of the Miller Range shear zone, central Transantarctic Mountains, Antarctica, and

- 948 implications for Neoproterozoic to early Paleozoic tectonics of the East Antarctic margin of
949 Gondwana. *Tectonics* 12, 1460-1478 (1993).
- 950 121. Van Schmus, W. R., McKenna, L. W., Gonzales, D. A., Fetter, A. H., & Rowell, A. J. U-Pb
951 geochronology of parts of the Pensacola, Thiel, and Queen Maud mountains,
952 Antarctica. *The Antarctic Region: Geological Evolution and Processes. Terra Antarctica*,
953 Siena 187, 200 (1997).
- 954 122. Stump, E. *The Ross Orogen of the transantarctic mountains*. Cambridge University Press
955 (1995).
- 956 123. Martin, A. P., Price, R. C., Cooper, A. F., & McCammon, C. A. Petrogenesis of the rifted
957 southern Victoria Land lithospheric mantle, Antarctica, inferred from petrography,
958 geochemistry, thermobarometry and oxybarometry of peridotite and pyroxenite xenoliths
959 from the Mount Morning eruptive centre. *Journal of Petrology* 56, 193-226 (2015).
- 960 124. Goodge, J. W., Myrow, P., Williams, I. S., & Bowring, S. A. Age and provenance of the
961 Beardmore Group, Antarctica: constraints on Rodinia supercontinent breakup. *The Journal*
962 *of geology* 110, 393-406 (2002).
- 963 125. Stump, E., Gehrels, G., Talarico, F. M., & Carosi, R. Constraints from detrital zircon
964 geochronology on the early deformation of the Ross orogen, Transantarctic Mountains,
965 Antarctica. In *Antarctica: A Keystone in a Changing World – Online Proceedings of the*
966 *10th ISAES*, edited by A.K. Cooper and C.R. Raymond et al., USGS Open-File Report
967 2007-1047, Extended Abstract 166 (2007).
- 968 126. Cooper, A. F., Maas, R., Scott, J. M., & Barber, A. J. Dating of volcanism and
969 sedimentation in the Skelton Group, Transantarctic Mountains: implications for the
970 Rodinia-Gondwana transition in southern Victoria Land, Antarctica. *GSA Bulletin* 123,
971 681-702 (2011).
- 972 127. Goodge, J. W., Fanning, C. M., & Bennett, V. C. U–Pb evidence of ~1.7 Ga crustal
973 tectonism during the Nimrod Orogeny in the Transantarctic Mountains, Antarctica:
974 implications for Proterozoic plate reconstructions. *Precambrian Research* 112, 261-288
975 (2001).
- 976 128. Goodge, J. W., & Fanning, C. M. Mesoarchean and Paleoproterozoic history of the Nimrod
977 Complex, central Transantarctic Mountains, Antarctica: stratigraphic revisions and relation
978 to the Mawson Continent in East Gondwana. *Precambrian Research* 285, 242-271 (2016).
- 979 129. Veevers, J. J., & Saeed, A. Age and composition of Antarctic bedrock reflected by detrital
980 zircons, erratics, and recycled microfossils in the Prydz Bay–Wilkes Land–Ross Sea–Marie
981 Byrd Land sector (70–240 E). *Gondwana Research* 20, 710-738 (2011).
- 982 130. Goodge, J. W., & Fanning, C. M. 2.5 by of punctuated Earth history as recorded in a single
983 rock. *Geology* 27, 1007-1010 (1999).
- 984 131. Grindley, G. W., McGregor, V. R., & Walcott, R. I. Outline of the geology of the Nimrod-
985 Beardmore-Axel Heiberg glaciers region, Ross Dependency. *Antarctic Geology*, 206-219
986 (1964).
- 987 132. Laird, M. G. The late Proterozoic-middle Palaeozoic rocks of Antarctica. In R. J. Tingey
988 (Ed.) *The Geology of Antarctica* (pp. 74-119). Oxford University Press, Oxford (1991).
- 989 133. Goodge, J. W., & Finn, C. A. Glimpses of East Antarctica: Aeromagnetic and satellite
990 magnetic view from the central Transantarctic Mountains of East Antarctica. *Journal of*
991 *Geophysical Research: Solid Earth* 115 (2010).

- 992 134. Goodge, J. W., & Fanning, C. M. Composition and age of the East Antarctic Shield in
993 eastern Wilkes Land determined by proxy from Oligocene-Pleistocene glaciomarine
994 sediment and Beacon Supergroup sandstones, Antarctica. *GSA Bulletin* 122, 1135-1159
995 (2010).
- 996 135. Gunn, B. M., & Warren, G. Geology of Victoria Land between the Mawson and Mulock
997 Glaciers, Antarctica. *New Zea. Geol. Bull.* 71, 157 (1962).
- 998 136. Encarnación, J., Rowell, A.J., Grunow, A.M. A U-Pb age for the Cambrian Taylor
999 Formation, Antarctica: Implications for the Cambrian time scale. *Journal of Geology* 107,
1000 497–504 (1999).
- 1001 137. Wareham, C. D., Stump, E., Storey, B. C., Millar, I. L., & Riley, T. R. Petrogenesis of the
1002 Cambrian Liv Group, a bimodal volcanic rock suite from the Ross orogen, Transantarctic
1003 Mountains. *Geological Society of America Bulletin* 113, 360-372 (2001).
- 1004 138. Elliot, D. H., Larsen, D., Fanning, C. M., Fleming, T. H., & Vervoort, J. D. The Lower
1005 Jurassic Hanson Formation of the Transantarctic Mountains: implications for the Antarctic
1006 sector of the Gondwana plate margin. *Geological Magazine* 154, 777-803 (2016).
- 1007 139. Elliot, D.H., Fanning, C.M., Isbell, J.L., Hulett, S.R.W. The Permo-Triassic Gondwana
1008 sequence, central Transantarctic Mountains, Antarctica: Zircon geochronology, provenance,
1009 and basin evolution. *Geosphere* 13, 155–178 (2017). <https://doi.org/10.1130/GES01345.1>.
- 1010 140. Elsner, M., Schöner, R., Gerdes, A., & Gaupp, R. (2013). Reconstruction of the early
1011 Mesozoic plate margin of Gondwana by U–Pb ages of detrital zircons from northern
1012 Victoria Land, Antarctica. *Geological Society, London, Special Publications*, 383(1), 211-
1013 232.
- 1014 141. Paulsen, T., Deering, C., Sliwinski, J., Bachmann, O., Guillong, M. New detrital zircon age
1015 and trace element evidence for 1450 Ma igneous zircon sources in East Antarctica.
1016 *Precambrian Res.* 300, 53–58 (2017). <http://dx.doi.org/10.1016/j.precamres.2017.07.011>
- 1017 142. Zurli, L. et al. Detrital zircons from Late Paleozoic Ice Age sequences in Victoria Land
1018 (Antarctica): New constraints on the glaciation of southern Gondwana. *GSA Bulletin*
1019 (2021) <https://doi.org/10.1130/B35905.1>
- 1020 143. Welke, B. et al. Applications of detrital geochronology and thermochronology from glacial
1021 deposits to the Paleozoic and Mesozoic thermal history of the Ross Embayment,
1022 Antarctica. *Geochemistry, Geophysics, Geosystems* 17, 2762-2780 (2016).
- 1023 144. Vogel, M. B., Ireland, T. R., & Weaver, S. D. The multistage history of the Queen Maud
1024 Batholith, La Gorce Mountains, central Transantarctic Mountains. In *Antarctica at the close*
1025 *of a millennium: proceedings of the 8th International Symposium on Antarctic Earth*
1026 *Sciences, Wellington 1999* (2002).
- 1027 145. Gootee, B., & Stump, E. Depositional environments of the Byrd Group, Byrd Glacier area:
1028 a Cambrian record of sedimentation, tectonism, and magmatism. In: Fütterer D.K.,
1029 Damaske D., Kleinschmidt G., Miller H. & Tessensohn F. (Eds.) *Antarctica*. Springer,
1030 Berlin, Heidelberg (2006).
- 1031 146. Barrett, P. J. The Devonian to Jurassic Beacon Supergroup of the Transantarctic Mountains
1032 and correlatives in other parts of Antarctica. In: *The geology of Antarctica*, 120-152 (1991).
- 1033 147. Ferraccioli, F., Armadillo, E., Jordan, T., Bozzo, E., & Corr, H. Aeromagnetic exploration
1034 over the East Antarctic Ice Sheet: a new view of the Wilkes Subglacial Basin.
1035 *Tectonophysics* 478, 62-77 (2009).

- 1036 148. Paxman, G. J. et al. Geology and Geomorphology of the Pensacola-Pole Basin, East
1037 Antarctica. *Geochemistry, Geophysics, Geosystems* 20, 2786-2807 (2019).
- 1038 149. Elliot, D. H. The Hanson Formation: a new stratigraphical unit in the Transantarctic
1039 Mountains, Antarctica. *Antarctic Science* 8, 389-394 (1996).
- 1040 150. Elliot, D. H., & Fleming, T. H. Occurrence and dispersal of magmas in the Jurassic Ferrar
1041 large igneous province, Antarctica. *Gondwana Research* 7, 223-237 (2004).
- 1042 151. Burgess, S. D., Bowring, S. A., Fleming, T. H., & Elliot, D. H. High-precision
1043 geochronology links the Ferrar large igneous province with early-Jurassic ocean anoxia and
1044 biotic crisis. *Earth and Planetary Science Letters* 415, 90-99 (2015).
- 1045 152. Encarnación, J., Fleming, T. H., Elliot, D. H., & Eales, H. V. Synchronous emplacement of
1046 Ferrar and Karoo dolerites and the early breakup of Gondwana. *Geology* 24, 535-538
1047 (1996).
- 1048 153. Cook, C. P. et al. Glacial erosion of East Antarctica in the Pliocene: A comparative study of
1049 multiple marine sediment provenance tracers. *Chemical Geology* 466, 199-218 (2017).
- 1050 154. Adams, C. J. Geochronological studies of the Swanson Formation of Marie Byrd Land,
1051 West Antarctica, and correlation with northern Victoria Land, East Antarctica, and South
1052 Island, New Zealand. *New Zealand Journal of Geology and Geophysics* 29, 345-358
1053 (1986).
- 1054 155. Yakymchuk, C. et al. Anatectic reworking and differentiation of continental crust along the
1055 active margin of Gondwana: a zircon Hf–O perspective from West Antarctica. *Geological
1056 Society, London, Special Publication* 383 (2013). <https://doi.org/10.1144/SP383.7>
- 1057 156. Yakymchuk, C. et al. Paleozoic evolution of western Marie Byrd Land, Antarctica. *GSA
1058 Bull.* 127, 1464–1484 (2015).
- 1059 157. Simões Pereira, P. et al. The geochemical and mineralogical fingerprint of West
1060 Antarctica's weak underbelly: Pine Island and Thwaites glaciers. *Chemical Geology*,
1061 119649 (2020).
- 1062 158. Adams, C. J. Geochronology of granite terranes in the Ford Ranges, Marie Byrd Land,
1063 West Antarctica. *New Zealand journal of geology and geophysics* 30, 51-72 (1987).
- 1064 159. LeMasurier, W. E. et al. (1990). *Volcanoes of the Antarctic Plate and Southern Ocean* (Vol.
1065 48). Washington, D.C., American Geophysical Union.
- 1066 160. Licht, K. J. et al. Evidence for extending anomalous Miocene volcanism at the edge of the
1067 East Antarctic craton. *Geophysical Research Letters* 45, 3009-3016 (2018).
- 1068 161. Brodie, J. W. A shallow shelf around Franklin Island in the Ross Sea, Antarctica. *New
1069 Zealand Journal of Geology and Geophysics* 2, 108-119 (1959).
- 1070 162. Lawver, L., Lee, J., Kim, Y., & Davey, F. Flat-topped mounds in western Ross Sea:
1071 Carbonate mounds or subglacial volcanic features? *Geosphere* 8, 645-653 (2012).
- 1072 163. Di Vincenzo, G., Bracciali, L., Del Carlo, P., Panter, K., & Rocchi, S. ⁴⁰Ar–³⁹Ar dating of
1073 volcanogenic products from the AND-2A core (ANDRILL Southern McMurdo Sound
1074 Project, Antarctica): correlations with the Erebus Volcanic Province and implications for
1075 the age model of the core. *Bulletin of Volcanology* 72, 487-505 (2010).
- 1076 164. Panter, K. S. et al. Melt origin across a rifted continental margin: a case for subduction-
1077 related metasomatic agents in the lithospheric source of alkaline basalt, NW Ross Sea,
1078 Antarctica. *Journal of Petrology* 59, 517-558 (2018).

- 1079 165. McIntosh, W. C. $^{40}\text{Ar}/^{39}\text{Ar}$ geochronology of tephra and volcanic clasts in CRP-2A,
1080 Victoria Land Basin, Antarctica. *Terra Antarctica* 7, 621-630 (2000).
- 1081 166. LeMasurier, W. E., & Rocchi, S. Terrestrial record of post-Eocene climate history in Marie
1082 Byrd Land, West Antarctica. *Geografiska Annaler: Series A, Physical Geography* 87, 51-66
1083 (2005).
- 1084 167. Rocchi, S., LeMasurier, W. E., & Di Vincenzo, G. (2006). Oligocene to Holocene erosion
1085 and glacial history in Marie Byrd Land, West Antarctica, inferred from exhumation of the
1086 Dorrel Rock intrusive complex and from volcano morphologies. *GSA Bull.* 118, 991-1005.
- 1087 168. LeMasurier, W. Shield volcanoes of Marie Byrd Land, West Antarctic rift: oceanic island
1088 similarities, continental signature, and tectonic controls. *Bulletin of Volcanology* 75, 726
1089 (2013).
- 1090 169. Behrendt, J. C. et al. Geophysical studies of the West Antarctic rift system. *Tectonics* 10,
1091 1257-1273 (1991).
- 1092 170. McDougall, I. & Harrison, T. M. *GEOCHRONOLOGY and THERMOCHRONOLOGY*
1093 *by the $^{40}\text{Ar}/^{39}\text{Ar}$ METHOD.* Oxford University Press, Oxford (1999).
- 1094 171. Cherniak, D. J., & Watson, E. B. Pb diffusion in zircon. *Chemical Geology* 172, 5-24
1095 (2001).
- 1096 172. Morrison A.D. & Reay A. Geochemistry of Ferrar Dolerite sills and dikes at Terra Cotta
1097 Mountain, south Victoria Land, Antarctica. *Antarctic Science* 7, 73-85 (1995).
- 1098 173. Cox, S.C., Turnbull, I.M., Isaac, M.J., Townsend, D.B. & Smith Lyttle, B. Geology of
1099 southern Victoria Land, Antarctica. Institute of Geological & Nuclear Sciences geological
1100 map 22, scale 1:250 000, 1 sheet (2012).
- 1101 174. Ford, A. B. Stratigraphy of the layered gabbroic Dufek intrusion, Antarctica. *U.S. Geol.*
1102 *Surv. Bull.*, vol. 1405-D (1976).
- 1103 175. Borg, S. G., Depaolo, D. J., & Smith, B. M. Isotopic structure and tectonics of the central
1104 Transantarctic Mountains. *Journal of Geophysical Research: Solid Earth* 95, 6647-6667
1105 (1990).
- 1106 176. Cox, S.C., Parkinson, D.L., Allibone, A.H. & Cooper, A.F. Isotopic character of Cambro-
1107 Ordovician plutonism, southern Victoria Land, Antarctica. *New Zealand Journal of*
1108 *Geology and Geophysics* 43, 501-520 (2000). DOI: 10.1080/00288306.2000.9514906.
- 1109 177. Gunner, J. *ISOTOPIC and GEOCHEMICAL STUDIES of the PRE-DEVONIAN*
1110 *BASEMENT COMPLEX, BEARDMORE GLACIER REGION, ANTARCTICA.* Ohio
1111 State University, Columbus, Institute of Polar Studies Report No. 41 (1976).
- 1112 178. Roy, M., van de Fliedert, T., Hemming, S. R., & Goldstein, S. L. $^{40}\text{Ar}/^{39}\text{Ar}$ ages of
1113 hornblende grains and bulk Sm/Nd isotopes of circum-Antarctic glacio-marine sediments:
1114 Implications for sediment provenance in the Southern Ocean. *Chemical Geology* 244, 507-
1115 519 (2007).
- 1116 179. Behrendt, J. C. The aeromagnetic method as a tool to identify Cenozoic magmatism in the
1117 West Antarctic Rift System beneath the West Antarctic Ice Sheet—A review; Thiel
1118 subglacial volcano as possible source of the ash layer in the
1119 WAISCOPE. *Tectonophysics* 585, 124-136 (2013).
- 1120 180. Lough, A. C. et al. Seismic detection of an active subglacial magmatic complex in Marie
1121 Byrd Land, Antarctica. *Nature Geoscience* 6, 1031-1035 (2013).

- 1122 181. Schroeder, D. M., Blankenship, D. D., Young, D. A., & Quartini, E. Evidence for elevated
1123 and spatially variable geothermal flux beneath the West Antarctic Ice Sheet. *Proceedings of*
1124 *the National Academy of Sciences* 111, 9070-9072 (2014).
- 1125 182. Ehrmann, W. U., Melles, M., Kuhn, G., & Grobe, H. Significance of clay mineral
1126 assemblages in the Antarctic Ocean. *Marine Geology* 107, 249-273 (1992).
- 1127 183. Fagel N. Clay minerals, deep circulation and climate. *Proxies Late Cenozoic*
1128 *Paleoceanogr.* 1, 139-184 (2007).
- 1129 184. Kristoffersen, Y., Strand, K., Vorren, T., Harwood, D. and Webb, P. Pilot shallow drilling
1130 on the continental shelf, Dronning Maud Land, Antarctica. *J. Antarct. Sci.* 4, 463–470
1131 (2000).
- 1132 185. Ehrmann, W. et al. Provenance changes between recent and glacial-time sediments in the
1133 Amundsen Sea embayment, West Antarctica: clay mineral assemblage evidence. *Antarctic*
1134 *Science* 23, 471-486 (2011).
- 1135 186. Hillenbrand, C. D., Grobe, H., Diekmann, B., Kuhn, G., & Fütterer, D. K. Distribution of
1136 clay minerals and proxies for productivity in surface sediments of the Bellingshausen and
1137 Amundsen seas (West Antarctica)—Relation to modern environmental conditions. *Marine*
1138 *Geology* 193, 253-271 (2003).
- 1139 187. Klages, J. P. et al. Temperate rainforests near the South Pole during peak Cretaceous
1140 warmth. *Nature* 580, 81-86 (2020).
- 1141 188. Zonneveld, K.A.F., Bockelmann, F. & Holzwarth, U. Selective preservation of organic-
1142 walled dinoflagellate cysts as a tool to quantify past net primary production and bottom
1143 water oxygen concentrations. *Marine Geology* 237, 109–126 (2007).
- 1144 189. Prebble, J. G., Hannah, M. J., & Barrett, P. J. (2006). Changing Oligocene climate recorded
1145 by palynomorphs from two glacio-eustatic sedimentary cycles, Cape Roberts Project,
1146 Victoria Land Basin, Antarctica. *Palaeogeogr., Palaeoclimatol., Palaeoecol.* 231, 58-70.
- 1147 190. Kulhanek, D.K. et al. Revised chronostratigraphy of DSDP Site 270 and late Oligocene to
1148 early Miocene paleoecology of the Ross Sea sector of Antarctica. *Global and Planetary*
1149 *Change* 178, 46-64 (2019).
- 1150 191. Feakins, S., Warny, S. & Lee, J.E. Hydrologic cycling over Antarctica during the middle
1151 Miocene warming. *Nature Geosci.* 5, 557–560 (2012). <https://doi.org/10.1038/ngeo1498>
- 1152 192. De Santis, L., Prato, S., Brancolini, G., Lovo, M., & Torelli, L. The Eastern Ross Sea
1153 continental shelf during the Cenozoic: implications for the West Antarctic ice sheet
1154 development. *Global and Planetary Change* 23, 173-196 (1999).
- 1155 193. Ford, A. B., & Barrett, P. J. Basement rocks of the south-central Ross Sea, Site 270, DSDP
1156 Leg 28. *Initial Reports of the Deep Sea Drilling Project* 28, 861-868 (1975).
- 1157 194. Goldich, S. S., Treves, S. B., Suhr, N. H., & Stuckless, J. S. Geochemistry of the Cenozoic
1158 volcanic rocks of Ross Island and vicinity, Antarctica. *The Journal of Geology* 83, 415-435
1159 (1975).
- 1160 195. Tulaczyk, S., Kamb, B., Scherer, R. P., & Engelhardt, H. F. Sedimentary processes at the
1161 base of a West Antarctic ice stream; constraints from textural and compositional properties
1162 of subglacial debris. *Journal of Sedimentary Research* 68, 487-496 (1998).
- 1163 196. Rosenqvist, I. T. Origin and mineralogy glacial and interglacial clays of southern
1164 Norway. *Clays and Clay Minerals* 23, 153-159 (1975).

- 1165 197. Blum, J. D., & Erel, Y. Rb/ Sr isotope systematics of a granitic soil chronosequence: The
1166 importance of biotite weathering. *Geochimica et Cosmochimica Acta* 61, 3193-3204
1167 (1997).
- 1168 198. Eisenhauer, A. et al. Grain size separation and sediment mixing in Arctic Ocean sediments:
1169 evidence from the strontium isotope systematic. *Chemical Geology* 158, 173-188 (1999).

1170 **Data availability** All data from this study can be found in the British Geological Survey National
1171 Geoscience Data Centre. (6 DOIs for Nd and Sr isotope, Zircon U-Pb, Clast, Clay Mineralogy,
1172 *Hornblende ⁴⁰Ar/³⁹Ar and Palynological data are currently being produced*).

1173 **Permit** Antarctic Conservation Act Permit Number: ACA 2018-027 (permit holder: Bradford
1174 Clement, JRSO, IODP, TAMU, College Station, TX 77845)

1175 **Acknowledgements**

1176 This research used data and samples provided by the International Ocean Discovery Program
1177 (IODP), which is sponsored by the US National Science Foundation (NSF) and participating
1178 countries under the management of Joint Oceanographic Institutions. J.W.M. was supported by a
1179 NERC DTP studentship. Neodymium and Sr isotope analysis and U-Pb dating of detrital zircons was
1180 funded through NERC UK IODP grant NE/R018219/1. Clast counts performed by L.Z., F.T. and
1181 M.P. and the participation of L.D. and F.C. was funded by the Italian National Antarctic Research
1182 Program (PNRA - Programma Nazionale Ricerche in Antartide) - grant numbers PNRA18-00233,
1183 PNRA16-00016 and PNRA18-00002. R.M.M. was supported by Royal Society Te Apārangi
1184 Marsden Fund (18-VUW-089). L.F.P. has been funded by the European Union's Horizon 2020
1185 research and innovation programme under the Marie Skłodowska-Curie grant agreement No. 792773
1186 WAMSISE. D.K.K. was supported by the IODP JOIDES Resolution Science Operator and National
1187 Science Foundation (grant 1326927). Southern Transantarctic Mountain rock samples for Nd and Sr
1188 isotope analysis were provided by the Polar Rock Repository with support from the National Science
1189 Foundation, under Cooperative Agreement OPP-1643713. We thank B. Coles, K. Kreissig and P.
1190 Simões Pereira for technical support. We also thank the numerous scientists who collected invaluable

1191 site survey data and developed the proposals and hypotheses that ultimately led to IODP Expedition
1192 374.

1193 **Author Contributions**

1194 J.W.M., T.v.d.F, R.M.M., L.D.S. and A.E.S. designed the research in collaboration with the entire
1195 IODP Expedition 374 science party. J.W.M. conducted the Nd and Sr isotope analyses. L.Z., F.T.
1196 and M.P. performed the clast counts. J.W.M., P.V. and A.C. produced the zircon U-Pb data. F.B. and
1197 V.B.R. collected the clay mineralogy data. F.S., J.P. and C.B. performed the palynological counts
1198 and interpretations. S.R.H. provided the hornblende $^{40}\text{Ar}/^{39}\text{Ar}$ data. K.J.L. provided guidance on
1199 geochronology interpretations. L.F.P., F.C. and L.D.S. calculated the sediment volume estimate. R.L,
1200 R.M.M., T.E.v.P., D.H., D.K.K. and E.M.G. improved the shipboard age model. N.B.S and S.R.M.
1201 conducted the astrochronological analyses. D.K.K. provided the XRF data. E.G. and B.K. helped
1202 integrate sediment provenance data with numerical modelling.////// I.B., G.K., and J.E.D. advised on
1203 specific technical aspects of the manuscript. J.W.M. created the figures and wrote the text with
1204 assistance from all authors and particular guidance from T.v.d.F, C.D.H, E.G., and M.J.S.. All
1205 Expedition 374 scientists contributed to the collection of shipboard datasets and the interpretations of
1206 the data.

1207 **Consortia**

1208 *IODP Expedition 374*

1209 Jeanine Ash, François Beny, Imogen M. Browne, Giuseppe Cortese, Laura De Santis, Justin P.
1210 Dodd, Oliver M. Esper, Jenny A. Gales, David M. Harwood, Saki Ishino, Benjamin A. Keisling,
1211 Sookwan Kim, Sunghan Kim, Denise K. Kulhanek, Jan Sverre Laberg, R. Mark Leckie, Robert M.
1212 McKay, Juliane Müller, Molly O. Patterson, Brian W. Romans, Oscar E. Romero, Francesca
1213 Sangiorgi, Osamu Seki, Amelia E. Shevenell, Shiv M. Singh, Isabela M. Cordeiro de Sousa, Saiko T.
1214 Sugisaki, Tina van de Flierdt, Tim E. van Peer, Whenshen Xiao and Zhifang Xiong.

1215 **Competing Interests** The authors declare no competing interests.

1216 Correspondence and requests for materials should be addressed to James W. Marschalek.

1217 **Extended Data Figure and Table Legends**

1218 **Extended Data Figure 1. Age model constraints below 75 mbsf at Site U1521.** From left to right
1219 are: depth (metres below sea floor), core number, core recovery (black = recovered), inclination prior
1220 to and after 10 and 20 mT demagnetisation (black, blue and red points, successively), and
1221 corresponding polarity interpretations (black = normal, white = reversed, grey = no interpretation).
1222 Note that the polarity interpretations have been simplified compared to those in the cruise report²⁶,
1223 with small uncertainties related to core gaps removed. Note Site U1521 is in the Southern
1224 Hemisphere. The geomagnetic polarity timescale⁴⁸ is shown across the top of the plot. The orange
1225 shaded regions indicate uncertainties in our age model and the dashed line marks an alternative line
1226 of correlation for Sequence 3. The blue line indicates the age model for Sequence 2 based on our
1227 astrochronological analyses, with the light blue shading indicating the ~20 kyr uncertainty associated
1228 with the phase relationship between clast abundances and obliquity. This astrochronological
1229 anchoring agrees closely with linear interpolations between magnetostratigraphic tie points (black
1230 line).

1231 **Extended Data Figure 2. Selected palynological counts compared to strontium and neodymium**
1232 **isotope data.** Palynological data are reported as percentages (crosses) and counts/gram (circles). The
1233 blue shaded area represents Sequence 2, which is interpreted as consisting of sediments with a West
1234 Antarctic provenance. Error bars indicate a 95% confidence interval⁴⁷.

1235 **Extended Data Figure 3. Down-core clast and clay mineral distribution.** The blue shaded area
1236 highlights Sequence 2, which is interpreted to consist of sediments with a West Antarctic
1237 provenance. a) Core lithology (see Figure 2 for key). b) Chronostratigraphic sequences. c) Clast

1238 abundance. d) Percentages of different clast lithologies. e) Ratio between dolerite and total number
1239 of clasts (red) and volcanic rocks and total number of clasts (green), with 95% confidence interval
1240 shown as pale shading⁴⁷. f) Clay mineral abundances.

1241 **Extended Data Figure 4. Map of approximate ϵ_{Nd} values in rocks and offshore sediments from**
1242 **around the Ross Sea embayment.** Epsilon Nd values are overlain on MODIS imagery²⁰⁹ and the
1243 BedMachine Antarctica V1 modern bed topography⁴³, with the MEaSURES grounding line and ice
1244 sheet margin shown^{44,45}. The approximate boundary between West and East Antarctic lithosphere is
1245 shown using a white dashed line⁴⁶. Modern/late Holocene and terrestrial till samples are represented
1246 by circles with the same colour bar^{28,30,54}. Although ice flow patterns have changed since their
1247 deposition, Last Glacial Maximum tills in offshore sediments are also plotted as squares to improve
1248 spatial coverage²⁸. Individual samples and references are reported in Supplementary Table 1. The
1249 bedrock map was produced by Kriging between sample locations within a group, then masking to the
1250 outcrop area. Beacon and Ferrar Group (Fig. 1) rocks are often not differentiated in geological
1251 mapping, but are roughly equal volumetrically¹³⁵, with the uppermost Beacon Supergroup formations
1252 having a Ferrar-like isotopic signature¹³⁸. We hence assume a 60% Ferrar, 40% Beacon mixture is
1253 representative.

1254 **Extended Data Figure 5. Kernel density estimate plots for literature measurements of rock ϵ_{Nd}**
1255 **compared to measurements on fine-grained Miocene detritus from Site U1521.** For references
1256 and a list of all the data, see Supplementary Table 1. The height of the curve indicates the density of
1257 measurements and n the total number of samples analysed. Colour scheme is identical to Figure 1,
1258 with sediments in grey.

1259 **Extended Data Figure 6. Kernel density estimates for hornblende $^{40}\text{Ar}/^{39}\text{Ar}$ ages compared to**
1260 **zircon U-Pb ages younger than 1500 Ma.** The two dating methods are show in red and blue,
1261 respectively. Bold letters correspond with those in Figure 3. The positions of major peaks and

1262 number of grains analysed are labelled in the corresponding colours. Stratigraphic position is shown
1263 in Figure 2.

1264 **Extended Data Figure 7. Close up of the Site U1521 interval with a West Antarctic provenance.**

1265 The stratigraphic log (a) is displayed alongside the percentage of reworked dinocysts (b), basalt clast
1266 fraction (c), relative abundance of smectite (d), Nd isotope data (e) and Fe/Ti ratios determined by X-
1267 ray fluorescence scanning (f).

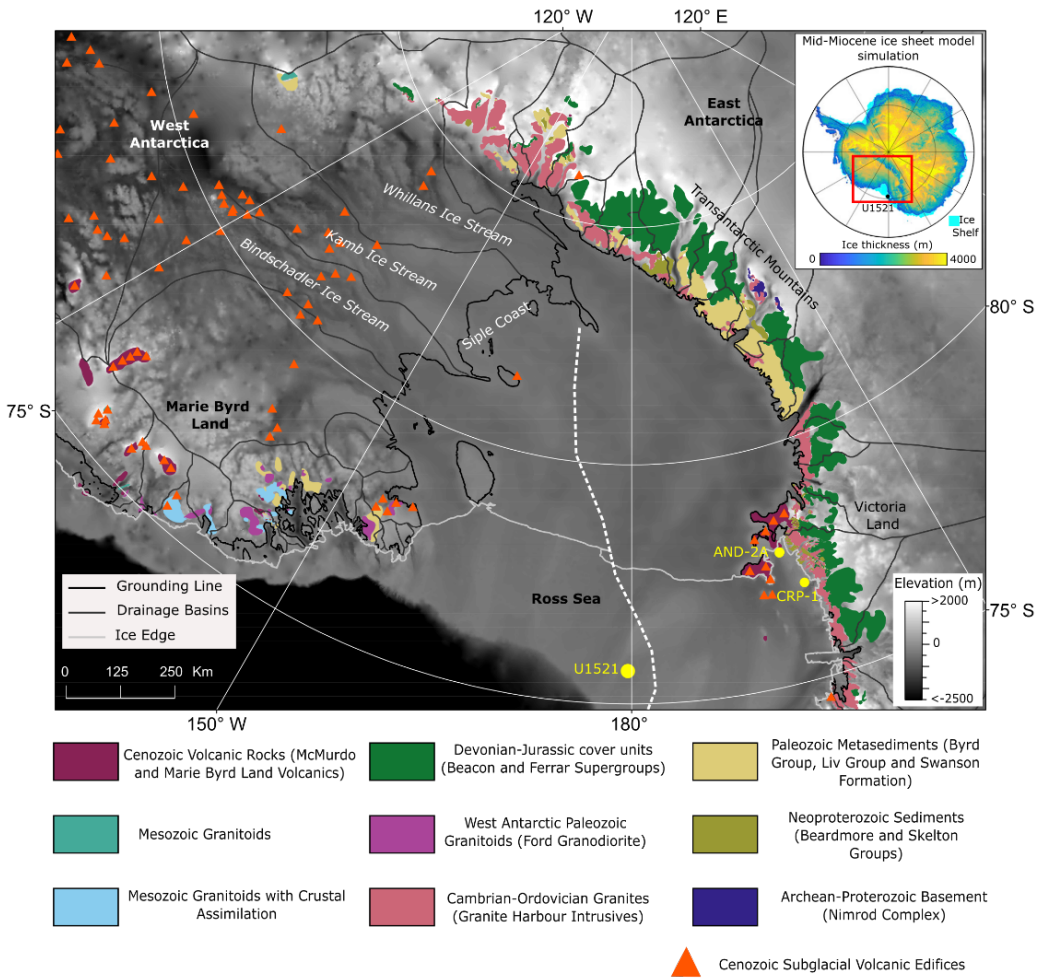
1268 **Extended Data Figure 8. Correlation of Site U1521 magnetostratigraphic tie points.** Shown are

1269 correlations between the AND-2A record¹¹, Site U1521²⁶ and the GPTS⁴⁸.

1270 **Extended Data Table 1. Age tie points for Site U1521 below 75 mbsf.** FAD: First Appearance

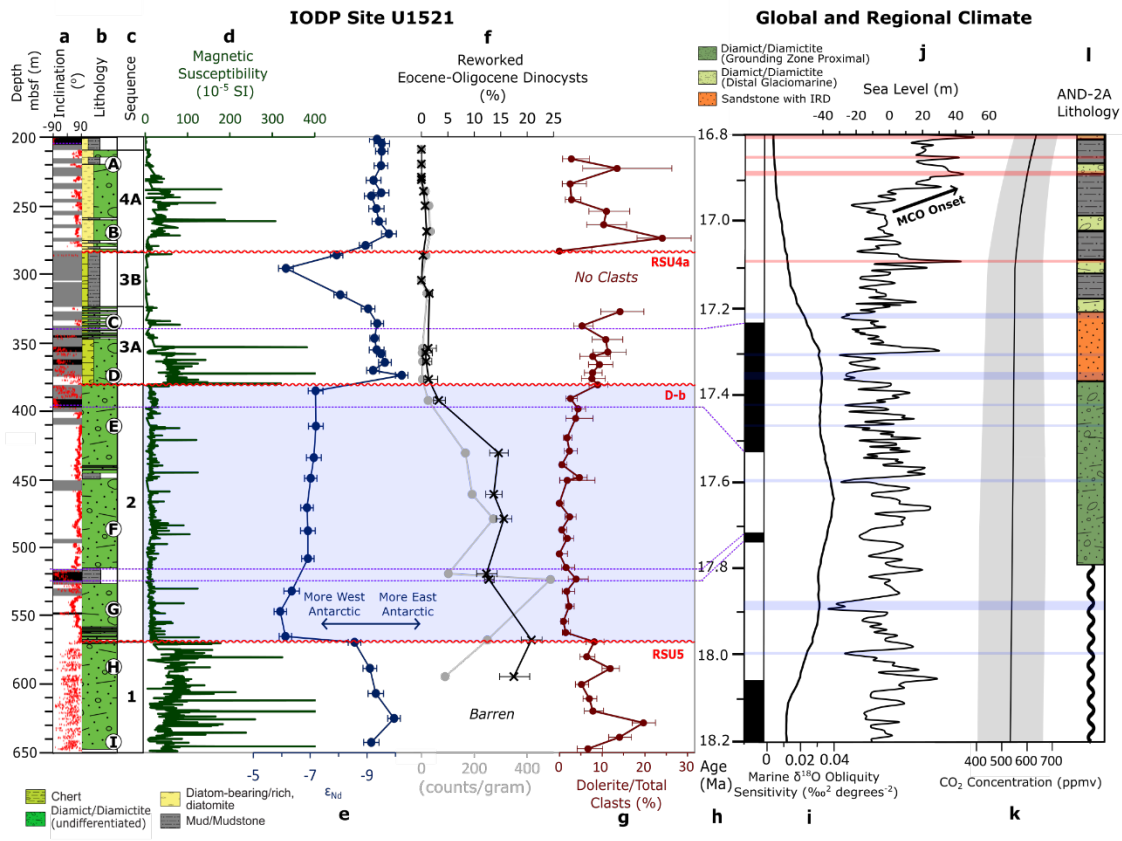
1271 Datum, LAD: Last Appearance Datum. Depth errors for the biostratigraphic datums reflect the
1272 position of the first downhole sample in which the reported species was not observed. We cannot
1273 exclude the possibility that the true first observation occurs between this sample and that reported as
1274 the FAD. Opal-CT indicates that the lowermost occurrence is uncertain due to poor preservation
1275 below the Opal-CT transition (~286.1 mbsf). Age errors for the biostratigraphic events are given as
1276 the maximum and minimum reported ages based on hybrid range models^{88,89}. Magnetic Polarity
1277 Reversals (MPR) depths are given as midpoints between samples with differing polarities, with the
1278 depth error indicating the distance to these samples.

1279 **Extended Data Table 2. Values used in the erosion rate calculation.**



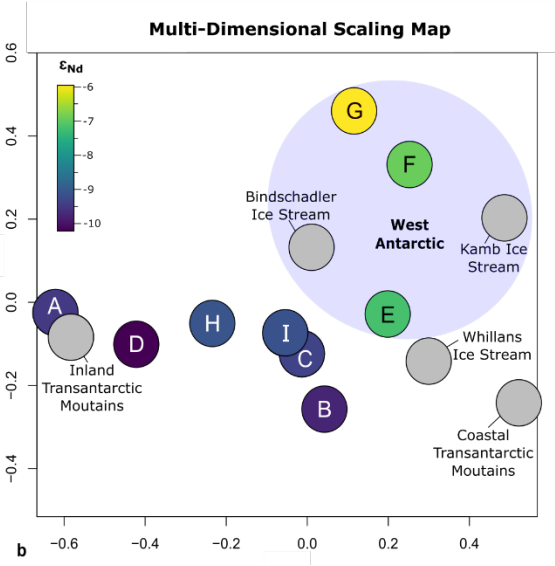
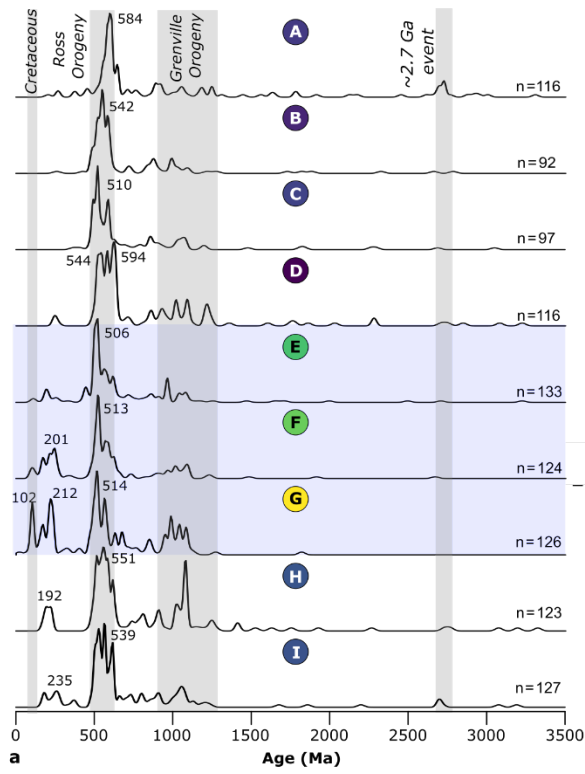
1280

1281



1282

1283



1284